# A theory of hydrogel mechanics that couples swelling and external flow

Zelai Xu[1], Pengtao Yue[2], and James J. Feng[1,3]

[1]Department of Chemical and Biological Engineering, University of British Columbia, Vancouver, BC V6T 1Z3, Canada
[3]Department of Mathematics, Virginia Tech, Blacksburg, VA 24061, USA
[3]Department of Mathematics, University of British Columbia, Vancouver, BC V6T 1Z2, Canada

### Abstract

Two aspects of hydrogel mechanics have been studied separately in the past. The first is the swelling and deswelling of gels in a quiescent solvent bath triggered by an environmental stimulus such as a change in temperature or pH, and the second is the solvent flow around and into a gel domain, driven by an external pressure gradient or moving boundary. The former neglects convection due to external flow, whereas the latter neglects solvent diffusion driven by a gradient in chemical potential. Motivated by engineering and biomedical applications where both aspects coexist and potentially interact with each other, this work presents a poroelasticity model that integrates these two aspects into a single framework, and demonstrates how the coupling between the two gives rise to novel physics in relatively simple one-dimensional and two-dimensional flows.

## 1 Introduction

Hydrogels are typically crosslinked polymer networks swollen by an aqueous solvent. They play increasingly important roles in engineering and biomedical applications, ranging from smart sensors and actuators [1,2] to organ-on-chip devices [3–5]. These applications take advantage of unique properties of hydrogels, including their biocompatibility, softness, permeability to solvent and biochemical factors, and sensitivity to changes of ambient conditions. For example, hydrogels can swell or shrink in response to changes in ambient temperature, pH levels, light, electric field or ionic strength [6–10], with novel applications in autonomous flow control [11, 12], wearable sensors and actuators [13] and soft electronics [14, 15]. They are also used extensively in *in vitro* assays as a supporting matrix or scaffold for growing and differentiating cells, and as a medium for administering growth factors or chemoattractants to the cells [16–18].

Mechanical modeling of hydrogels has largely been focused on their swelling and deswelling behavior in response to changes in the environment, e.g., in temperature or ionic strength. The gel is typically surrounded by a stationary solvent, with no externally induced flow. The environmental stimulus disrupts the chemical equilibrium between the gel and the surrounding medium, and a gradient of chemical potential then drives the solvent into the polymer network (swelling) against the elasticity of the network or out (deswelling). This process has been elegantly modeled by Hong *et al.* [19], and the same theoretical framework has been applied to explain how gels respond to

various environmental stimuli [10, 20–29]. In this context, one notes two equivalent descriptions of the solvent transport. The diffusive description adopts Fick's law, making the solvent flux proportional to the spatial gradient of a chemical potential, with a diffusivity coefficient [19, 24]. The alternative description uses Darcy's law, making the flux proportional to the spatial gradient of an osmotic pressure, with a permeability coefficient [20, 25, 30–32]. Insofar as the chemical potential and the osmotic pressure are essentially synonymous, and the diffusivity and permeability are both phenomenological material properties on the continuum level, these two descriptions are equivalent [10]. Note, however, that such a Darcian description does not represent the Darcy flow in the classical sense, driven by an *external* pressure gradient. As in the diffusive description, there is no momentum balance for the solvent inside the gel, and the solid momentum equation, $\nabla \cdot \boldsymbol{\sigma}_s = 0$, allows no influence from the solvent [10, 29]. Therefore, nomenclature notwithstanding, this series of studies has focused on *diffusive solvent transport* only.

Complementary to the above, *convective solvent transport* takes place owing to an external flow driven by a pressure gradient or boundary motion as in classical fluid mechanics. This process has been a mainstay in the mechanics of porous media [33–35], but has received relatively little attention for hydrogels [36]. Part of the reason is the difficulty in posing boundary conditions (BCs) on the interface between the hydrogel and the clear liquid, which play a central role in mediating the solvent transports inside the gel and outside [37–40]. Using irreversible thermodynamics, we have proposed such BCs and tested them in relatively simple flows involving a solvent-gel interface [41–43]. These results clearly suggest the importance of convection as a distinct mode of solvent transport, which may give rise to novel phenomena. For example, as the flow compresses the gel in a capillary, the solvent flux may vary non-monotonically with the pressure drop [44]. Flow-induced gel compression and expansion have also been implicated in kidney disease [45].

Is there value in integrating the diffusive and convective mechanisms of solvent transport into a single unified theory? There are emerging applications in which both act simultaneously, and potentially interact with each other. A prominent example is hydrogel-based actuators in microfluidic chips. The gel component swells or shrinks in response to changes in the surrounding fluid, e.g., in pH or temperature, thus effecting autonomous flow control by closing or opening microvalves [11, 12, 46–48]. Another notable application is wet-spinning of hydrogels of nanocellulose and nanochitin into filaments [49, 50]. The gel is stretched and pulled through a bath of coagulant or antisolvent, which extracts the solvent from the gel to produce a solid fiber. In such processes, both chemically driven diffusion and mechanically driven external flow play critical roles.

There has been little effort at integrating these two complementary mechanisms of solvent transport. Bacca and McMeeking [51] developed a viscoelastic model for gels by adding a viscous stress due to the solvent to the elastic stress due to the polymer network. But the solvent is assumed to deform affinely with the solid network, and thus no interstitial flow is allowed. More recently, Celora *et al.* [29] presented a comprehensive model for the swelling of polyelectrolyte gels with multicomponent diffusion of ions. In the solvent bath surrounding the gel domain, a viscous stress tensor is written out, formally allowing an external flow. Inside the gel, however, the solvent transport is entirely by Fickian diffusion. In the end, the model is applied to a polyelectrolyte gel swelling in a stationary solvent bath.

In this paper, we seek to integrate convective and diffusive solvent transport into a single theory, and then use it to explore dynamics of hydrogels in which both play active roles. A cornerstone of our model is a generalized Maxwell-Stefan equation that expresses the total flux as the sum of a convective flux and a diffusive flux. Only the former contributes to the Darcy drag in the momentum equations. Another novelty is

the boundary conditions for the interface between the gel and the solvent bath. From a thermodynamic argument, we derive BCs that relate the velocity jumps across the interface to jumps in the traction and the chemical potential. The model will be applied to one- and two-dimensional (1D and 2D) problems to demonstrate its utility and probe the interplay between the two mechanisms of solvent transport.

# 2 Model formulation

We consider a hydrogel immersed in a flowing solvent, where it swells or deswells by absorbing or exuding fluid while also deforming due to the external flow of the solvent. Thus, the dynamics of the hydrogel is affected by both diffusion and convection of the solvent. We account for the former by Fickian diffusion driven by the gradient of the chemical potential, and the latter as interstitial flow governed by poroelastic mechanics. The hydrogel is composed of a solid and a fluid phase, with volume fractions $\phi_s$ and $\phi_f$, respectively, such that $\phi_f + \phi_s = 1$. $\phi_f$ is also commonly called the porosity. The external flow is governed by the Stokes equations, with inertia neglected. On the interface between the hydrogel and the external fluid, we adopt a novel boundary condition on the solvent flux.

## 2.1 Chemical potential and Fickian flux

The formulation below follows mostly Hong *et al.*'s [19] model for hydrogel swelling in a quiescent solvent bath. The starting point is a free energy for the solvent and polymer mixture:

$$W_m = -m \left[ vC \ln \left( 1 + \frac{1}{vC} \right) + \frac{\chi}{1 + vC} \right], \qquad (1)$$

where $m$ indicates the magnitude of the free energy, $v$ is the volume of the solvent molecule, and $C$ is the solvent number concentration per unit volume of the dry polymer. Thus, the solvent volume fraction is $\phi_f = vC/(1 + vC)$. The first term inside the brackets represents the entropy of mixing, and the second term represents the enthalpy of mixing, where $\chi$ is a dimensionless parameter representing the hydrophilicity of the polymer network. The enthalpy of the hydrogel promotes solvent absorption if $\chi < 0$, and desorption if $\chi > 0$. We define the chemical potential as $\mu_m(C) = \partial W_m/\partial C$, and rewrite it in terms of $\phi_f$:

$$\mu_m(\phi_f) = mv \left[ \ln \phi_f + (1 - \phi_f) + \chi(1 - \phi_f)^2 \right]. \qquad (2)$$

In the original Flory-Huggins mixing energy [19, 52, 53], the parameter $m = k_B T/v$, with $k_B$ being the Boltzmann constant and $T$ the absolute temperature. In reality, $T$ may affect the gel in multiple ways, including via $m$, $\chi$ and the rigidity of the polymer network. For simplicity, we will disregard the specific physical mechanisms by which an environmental stimulus may affect the chemical potential $\mu_m$. Instead, we will treat $m$ as a generic measure of $\mu_m$, and vary $m$ as the simplest way of effecting changes in $\mu_m$. Note, however, that pH changes cannot be accommodated by the above free energy; the ionic transport and electrostatic interactions must be included explicitly [29].

Following Hong *et al.* [19], we write Fick's law for the number of solvent molecules crossing a unit area per unit time as

$$\mathbf{j}_i = -\frac{CD}{mv} \frac{1}{J} \nabla \mu_m = -\frac{D\phi_f}{mv^2} \nabla \mu_m, \qquad (3)$$

where $D$ is a constant diffusivity, $J = \det(\mathbf{F})$ is the Jacobian of solid deformation, $\mathbf{F} = \mathbf{I} + \hat{\nabla} \mathbf{u}_s$ being the solid deformation gradient tensor, with the gradient $\hat{\nabla}$ differentiating

the solid displacement $\mathbf{u}_s$ in the Lagrangian frame attached to the solid phase [42]. Thus, $J = 1/\phi_s$ is the gel volume expansion relative to the dry-polymer reference state, which has zero strain and zero stress. Now the volume flux of the solvent is

$$\mathbf{j}_f = v\mathbf{j}_i = -\frac{\phi_f D}{mv}\nabla\mu_m. \tag{4}$$

Using the chemical potential $\mu_m(\phi_f)$ of Eq. (2), we rewrite the Fickian flux as

$$\mathbf{j}_f = -D(1 - \phi_f)(1 - 2\chi\phi_f)\nabla\phi_f. \tag{5}$$

If we consider the prefactors multiplied onto $\nabla\phi_f$ to be a "diffusivity", then that diffusivity is non-constant for a constant $D$.

Here we note a departure from Hong *et al.*'s nomenclature [19]. To enforce "molecular incompressibility" of the solid and liquid, Hong *et al.* introduced an osmotic pressure $\Pi$ as a Lagrange multiplier, and appended it to the chemical potential $\mu_m$ of Eq. (2). Since we will add solvent convection into the model, the continuity equation will also require a hydrodynamic pressure as Lagrange multiplier. Thus, we have left $\Pi$ out of $\mu_m$, and will include it into a single $p$ that contains both hydrodynamic and osmotic pressures. This will become clearer when we introduce the generalized Maxwell-Stefan equation next.

## 2.2 The generalized Maxwell-Stefan equation

Conceptually, the task of integrating convective and diffusive solvent fluxes appears straightforward. The total solvent flux should consist of a convective component determined by the mechanics of the external flow, and a diffusive component given by Fick's law. A complication arises as diffusion of matter generates "flow" or "convection", and the Fickian flux is traditionally written as relative to an *average velocity* between the two diffusing species [54, 55]. There is much ambiguity in choosing such an average velocity in general [29, 55], and the issue is further complicated by an externally driven convection.

As a starting point, let us review the classical formulation of Fickian diffusion in the absence of an externally driven flow [54]. For the solvent and solid network of the gel, we denote their respective intrinsic phase-averaged velocity by $\mathbf{v}_f$ and $\mathbf{v}_s$, each defined by averaging over a sufficiently small volume that contains only the fluid or the solid [39]. Then an average velocity can be defined as $\mathbf{v} = \phi_f\mathbf{v}_f + \phi_s\mathbf{v}_s$, and the flux of each species is written as

$$\mathbf{q}_f = \phi_f\mathbf{v}_f = \phi_f\mathbf{v} + \mathbf{j}_f, \tag{6}$$
$$\mathbf{q}_s = \phi_s\mathbf{v}_s = \phi_s\mathbf{v} + \mathbf{j}_s, \tag{7}$$

with $\mathbf{j}_f = -\mathbf{j}_s$ being the diffusive flux according to Fick's law. It appears difficult to adapt this textbook formulation to accommodate an external flow. The average velocity $\mathbf{v}$ represents the movement of the center of volume of both species, and cannot reflect the motion of the solvent *relative* to the solid network. This can be seen more clearly by eliminating $\mathbf{v}$ between Eqs. (6) and (7) to arrive at the Maxwell-Stefan equation [55]:

$$\mathbf{v}_f - \mathbf{v}_s = \frac{\mathbf{j}_f}{\phi_f\phi_s}. \tag{8}$$

In the formulation of Eqs. (6, 7), therefore, the relative motion between the two phases can only be due to Fickian diffusion $\mathbf{j}_f$, and cannot be externally driven.

The conceptually opposite "convective limit" is where no diffusion exists ($\mathbf{j}_f = 0$) and the interstitial flow ($\mathbf{v}_f - \mathbf{v}_s$) is driven by a pressure gradient $-\nabla p$ according to Darcy's law:

$$\phi_f(\mathbf{v}_f - \mathbf{v}_s) = -\frac{k}{\mu}\nabla p, \tag{9}$$

where $\mu$ is the solvent viscosity, and $k$ is the classical Darcy permeability, which is a function of the porosity and pore geometry. As hydrogels typically have high porosity [44, 56–58], one may compute $k$ from Stokes flows through a dilute array of spherical particles of radius $r$ [59, 60]:

$$k = \frac{2r^2}{9}\frac{\phi_f}{\phi_s}, \tag{10}$$

This permeability will be used in the rest of the paper.

To unify the two limits of pure diffusion and pure convection, we postulate the following on the basis of Eqs. (8) and (9):

$$\mathbf{v}_f - \mathbf{v}_s = \frac{\mathbf{j}_f}{\phi_f\phi_s} - \frac{k}{\mu\phi_f}\nabla p, \tag{11}$$

which may be called the generalized Maxwell-Stefan equation. It will replace Darcy's law as the momentum equation for the interstitial fluid in our unified model.

We should note that Eq. (11) is not completely new; it has appeared in somewhat different forms in other contexts. In reverse osmosis and ultrafiltration, for example, Cussler [55] derived a similar relationship by formulating the Fickian flux of each phase relative to the solvent velocity. In concentrated suspensions that undergo flow and diffusion, Peppin *et al.* [61] argued for an equivalency between Darcy's law and Fick's law, recasting both into a "modified Darcy's law" of a similar form. Hennessy *et al.* [28] added a "mechanical pressure" to the osmotic pressure in the chemical gradient, thus arriving at a solvent flux that resembles Eq. (11).

## 2.3 Governing equations

The solvent and solid fluxes, $\phi_f\mathbf{v}_f$ and $\phi_s\mathbf{v}_s$, each implicitly contain a convective and a diffusive contribution, but these do not appear explicitly in the continuity equations:

$$\frac{\partial \phi_f}{\partial t} + \nabla \cdot (\phi_f\mathbf{v}_f) = 0, \tag{12}$$

$$\frac{\partial \phi_s}{\partial t} + \nabla \cdot (\phi_s\mathbf{v}_s) = 0. \tag{13}$$

The sum of the two equations gives a divergence-free condition for the average velocity: $\nabla \cdot (\phi_f\mathbf{v}_f + \phi_s\mathbf{v}_s) = 0$.

As in prior poroelastic models [36, 42, 43, 62], the momentum equations are essentially statements of force balance in the absence of inertia. For the solvent phase, we ignore the Brinkman term as scaling arguments show that the viscous stress can be dropped in favor of the Darcy drag [63]. This is commonly done in poroelastic models [29, 36]. Thus, the solvent executes Darcy flow. But Darcy's law must be replaced in our context by the generalized Maxwell-Stefan equation:

$$\nabla p = -\frac{\mu\phi_f}{k}(\mathbf{v}_f - \mathbf{v}_s) + \frac{\mu}{k\phi_s}\mathbf{j}_f. \tag{14}$$

In place of the solid-phase momentum equation, we adopt the total force balance for both phases [36, 62]:

$$\nabla \cdot (\phi_s\boldsymbol{\sigma}_s - p\mathbf{I}) = 0, \tag{15}$$

where $\boldsymbol{\sigma}_s$ is the solid stress tensor, and $\phi_s\boldsymbol{\sigma}_s$ is Terzaghi's effective stress [36]. The solid velocity $\mathbf{v}_s$ is related to the solid displacement $\mathbf{u}_s$ by $\mathbf{v}_s = d\mathbf{u}_s/dt$. For the solid stress $\boldsymbol{\sigma}_s$, we adopt the neo-Hookean elasticity model:

$$\boldsymbol{\sigma}_s = \mu_s J^{-1}(\mathbf{F}\cdot\mathbf{F}^T - \mathbf{I}) + \lambda_s(J-1)\mathbf{I}, \tag{16}$$

where $\mu_s$ and $\lambda_s$ are the Lamé constants of the solid network phase. The neo-Hookean model is more general than the linear or weakly nonlinear models of earlier studies, e.g., [19,31,64]. Note also that $\boldsymbol{\sigma}_s$ contributes to the overall force balance of the gel via the Terzaghi stress $\phi_s\boldsymbol{\sigma}_s$, whereas prior models often adopted an elastic stress tensor for the entire gel as a continuum.

The external flow is treated as inertialess Stokes flow:

$$\nabla \cdot \mathbf{V} = 0, \tag{17}$$

$$\nabla \cdot (\boldsymbol{\Sigma} - P\mathbf{I}) = 0, \tag{18}$$

where $\mathbf{V}$ and $P$ denote the velocity and pressure of the external fluid, and $\boldsymbol{\Sigma} = \mu[\nabla\mathbf{V} + (\nabla\mathbf{V})^T]$ is the viscous stress tensor with the fluid viscosity $\mu$.

## 2.4 Boundary conditions

Two general BCs come from the continuity of fluid flow and total traction balance on the interface between the hydrogel and the solvent outside:

$$\mathbf{n}\cdot(\mathbf{V} - \mathbf{v}_s) = \phi_f\mathbf{n}\cdot(\mathbf{v}_f - \mathbf{v}_s), \tag{19}$$

$$\mathbf{n}\cdot(\boldsymbol{\Sigma} - P\mathbf{I}) = \mathbf{n}\cdot(\phi_s\boldsymbol{\sigma}_s - p\mathbf{I}), \tag{20}$$

where $\mathbf{n}$ is the outward normal vector on the hydrogel surface. Equation (19) ensures volume conservation of fluid flowing through the interface. Equation (20) represents the balance of the tractions on both sides of the interface, where we have neglected the surface tension and the Brinkman viscous stress. However, additional boundary conditions are needed as both the fluid and solid phases in the gel have their own momentum equation.

In the convective limit ($\mathbf{j}_f = 0$), Young *et al.* [40,41,43] used the principle of positive entropy production to derive the following BCs:

$$\mu(\mathbf{V} - \mathbf{v}_s)\cdot\mathbf{n} = \eta(\mathbf{n}\cdot\boldsymbol{\Sigma}\cdot\mathbf{n} - P + p), \tag{21}$$

$$\mu(\mathbf{V} - \mathbf{v}_s)\cdot\mathbf{t} = \beta\,\mathbf{n}\cdot\boldsymbol{\Sigma}\cdot\mathbf{t}, \tag{22}$$

where $\mathbf{t}$ is the tangential vector along the interface, and the positive coefficients $\eta$ and $\beta$ are the interfacial penetration length and slip length, respectively. These conditions correspond to BC2 of [41,43], with some notational simplifications as explained in Appendix A. For the current purpose, we follow a similar procedure to extend Eq. (21) to account for diffusive flux across the gel-solvent interface (see Appendix A for details). The new BC thus derived is:

$$\mu(\mathbf{V} - \mathbf{v}_s)\cdot\mathbf{n} = \eta\left(\mathbf{n}\cdot\boldsymbol{\Sigma}\cdot\mathbf{n} - P + p + \frac{\mu_m}{v}\right). \tag{23}$$

Now Eqs. (19), (20), (22) and (23) form the complete set of BCs. The "interfacial penetration" BC of Eq. (23) states explicitly that the solvent flux across the interface depends on the jump in the fluid normal stress as well as the jump in chemical potential. During swelling of the hydrogel, the solvent diffuses into the gel where the chemical potential is lower ($\mu_m < 0$). Meanwhile, an externally imposed normal stress may inject the solvent into the gel. The solvent flux is the sum of both effects, with $\mu/\eta$ representing the resistance to the interfacial transport.

## 2.5 Comparison with previous models

In the above, we have formulated a model that integrates solvent convection and diffusion in hydrogels via the governing equations and the new boundary condition. It may be interesting to point out some connections to and distinctions from prior poromechanical models.

In the governing equations, the key difference is the inclusion of the fluid mechanics for the interstitial flow inside the gel. This necessitates a separate momentum equation for the pore fluid, and an explicit account of the solvent flux as the sum of a diffusive and a convective part (Eq. 11). If we neglect the interstitial fluid mechanics and set the flow outside the gel to nil, we recover the gel-swelling models in a quiescent solvent bath [10, 19, 25]. The generalized Maxwell-Stefan equation is algebraically similar to the expression for the diffusive flux in swelling models, e.g., [19, 65, 66]. Typically, these models add an osmotic pressure $\Pi$ to the chemical potential of our Eq. (2), such that the solvent flux equals our Eq. (4) plus an extra term proportional to $\nabla\Pi$. Insofar as $\Pi$ and our $p$ are both Lagrange multipliers to enforce volume conservation, the two formulations are algebraically equivalent. One subtle distinction is that in prior swelling models, the coefficients before the $\nabla\mu_m$ and $\nabla\Pi$ terms are related (see Eq. 22 of Drozdov *et al.* [66]). There is essentially one coefficient, which allows the flux to be interpreted as either Fickian or Darcian. In our Eq. (11), however, the diffusivity $D$ and hydraulic permeability $k$ are two independent parameters. This provides a means to distinguish the two kinds of fluxes unequivocally, even with simultaneous external flow and solvent diffusion.

The BCs on the gel-solvent interface is another essential element of our model, and such interfacial transport is especially important when solvent convection is included [29]. Most studies of gel swelling due to solvent diffusion, e.g., [19, 25, 28, 29], have imposed continuity of chemical potential as a boundary condition on the surface of the gel. In our notation, their BC amounts to

$$P - p - \frac{\mu_m}{v} = 0, \tag{24}$$

signifying instantaneous equilibration between the pressure jump and the chemical potential jump. An exception is the BC of Liu *et al.* [67],

$$P - p - \frac{\mu_m}{v} = -\frac{1}{m^c}\mathbf{n} \cdot \mathbf{v}_f, \tag{25}$$

which makes the solvent flux proportional to the interfacial jumps in pressure and the chemical potential. It is interesting to compare the BCs above with the diffusion-only limit of our interfacial penetration BC of Eq. (23), which can be realized by setting $\mathbf{V}$ and $\mathbf{\Sigma}$ to 0 (no external flow). Using the volume conservation of Eq. (19), we reduce Eq. (23) to

$$P - p - \frac{\mu_m}{v} = -\frac{\phi_f}{\phi_s}\frac{\mu}{\eta}\mathbf{n} \cdot \mathbf{v}_f. \tag{26}$$

The diffusion limit of our BC, therefore, is essentially the BC of Eq. (25) but differs from the commonly used Eq. (24); the latter can be recovered by taking the additional limit of large interfacial penetration $\eta \to \infty$.

Incidentally, Eq. (24) incurs a singularity when applied to gel swelling after a sudden change in the environment. This implies a sudden change in $\mu_m$ and, via Eq. (24), a sudden change in the pressure drop $P - p$ across the interface. From the interfacial traction balance (Eq. 20), this implies in turn a sudden change in the solid normal stress: $\phi_s\sigma_{snn} = -\mu_m/v$. This would require an instantaneous strain in the solid, with solid velocity $\mathbf{v}_s \to \infty$. In previous studies, one usually avoids the initial singularity

by starting the modeling with a pre-established solid stress [10, 19, 25]. Our new BC of Eq. (23), and its diffusion-only limit of Eq. (26), do not suffer from such a singularity, nor does Eq. (25).

## 2.6 Scaling

The permeability function of Eq. (10) invokes the pore size $r$, which is not explicitly accounted for in a homogenized theory such as poroelasticity. Therefore, we take the characteristic permeability $k^* = 2r^2/9$ as a phenomenological constant of the porous medium. Then our problem has 10 physical parameters, $k^*$, $\mu$, $\mu_s$, $\lambda_s$, $\eta$, $\beta$, $\chi$, $D$, $m$ and $\phi_{f0}$, and at least 1 geometric parameter $L_0$. The initial porosity $\phi_{f0}$ sets a uniform level of the chemical potential inside the gel, in equilibrium with the exterior. After a sudden change in ambient condition, $\mu_m$ jumps to a new value inside the gel to prompt swelling or deswelling. The physical setup may be such that we prescribe either a pressure drop $P_0$ or a far-field velocity $V_0$. For the time being, let us take $V_0$ as a prescribed parameter. Thus, we expect 9 dimensionless groups from the 12 parameters. Adopting $L_0$ as the characteristic length, $V_c = \mu_s k^*/(\mu L_0)$ as the characteristic velocity, and the network modulus $\mu_s$ as the characteristic stress, we scale the variables as follows to render the governing equations and BCs dimensionless:

$$(\bar{x}, \bar{y}) = (x, y)/L_0, \quad (\bar{\mathbf{V}}, \bar{\mathbf{v}}_s, \bar{\mathbf{v}}_f) = (\mathbf{V}, \mathbf{v}_s, \mathbf{v}_f)/V_c, \quad \bar{t} = tV_c/L_0,$$
$$\bar{\mathbf{u}}_s = \mathbf{u}_s/L_0, \quad (\bar{\boldsymbol{\sigma}}_s, \bar{\boldsymbol{\Sigma}}, \bar{P}, \bar{p}) = (\boldsymbol{\sigma}_s, \boldsymbol{\Sigma}, P, p)/\mu_s, \tag{27}$$

where the overbar denotes the dimensionless variables. The characteristic velocity $V_c$ is based on the ratio between the network rigidity and the Darcy drag. We prefer $V_c$ to the more obvious choices, the convection velocity $V_0$ and diffusion velocity $D/L_0$, as these cannot accommodate the diffusion-only and convection-only limits in a unified formulation. For convenience in parametric studies, we choose the following 9 dimensionless groups:

$$\bar{\lambda}_s = \lambda_s/\mu_s, \quad (\bar{\eta}, \bar{\beta}) = (\eta, \beta)\mu_s/(\mu V_c), \quad \bar{m} = m/\mu_s,$$
$$\bar{V}_0 = V_0/V_c, \quad \bar{\Delta} = D/(L_0 V_c), \quad \bar{K} = k^*/L_0^2, \quad \chi, \quad \phi_{f0}. \tag{28}$$

Some combinations of the groups have familiar physical meanings. For instance, $\bar{V}_0/\bar{\Delta} = LV_0/D$ forms a Péclet number, representing the ratio of the convective solvent flux to the diffusive solvent flux of Eq. (5). $\bar{V}_0\bar{K} = \mu V_0/(\mu_s L_0)$ is the ratio between the viscous stress in the fluid and the elastic stress in the solid network, and can be viewed as an effective capillary number. Finally, $\bar{\eta} = \eta L_0/k^*$ is the ratio between the interfacial penetration to the bulk permeability. This will be a key parameter to solvent transport.

In discussing the results, we use only dimensionless quantities and thus will omit the overbar hereafter. Substituting $\mu_m$ (Eq. 2), $\mathbf{j}_f$ (Eq. 5) and $k = k^*\phi_f/\phi_s$ (Eq. 10) into the fluid momentum equation, we summarize the dimensionless governing equations as

follows:

$$\frac{\partial \phi_f}{\partial t} + \nabla \cdot (\phi_f \mathbf{v}_f) = 0, \tag{29}$$

$$\frac{\partial \phi_s}{\partial t} + \nabla \cdot (\phi_s \mathbf{v}_s) = 0, \tag{30}$$

$$\nabla p = -\phi_s(\mathbf{v}_f - \mathbf{v}_s) - \Delta \frac{\phi_s(1 - 2\chi\phi_f)}{\phi_f} \nabla \phi_f, \tag{31}$$

$$\nabla \cdot (\phi_s \boldsymbol{\sigma}_s - p\mathbf{I}) = 0, \tag{32}$$

$$\boldsymbol{\sigma}_s = \phi_s(\mathbf{F} \cdot \mathbf{F}^T - \mathbf{I}) + \lambda_s \frac{\phi_f}{\phi_s} \mathbf{I}, \tag{33}$$

$$\nabla \cdot \mathbf{V} = 0, \tag{34}$$

$$\nabla P = K \nabla^2 \mathbf{V}. \tag{35}$$

The boundary conditions on the gel-fluid interface are:

$$\mathbf{n} \cdot (\mathbf{V} - \mathbf{v}_s) = \phi_f \mathbf{n} \cdot (\mathbf{v}_f - \mathbf{v}_s), \tag{36}$$

$$\mathbf{n} \cdot (\boldsymbol{\Sigma} - P\mathbf{I}) = \mathbf{n} \cdot (\phi_s \boldsymbol{\sigma}_s - p\mathbf{I}), \tag{37}$$

$$\mathbf{n} \cdot (\mathbf{V} - \mathbf{v}_s) = \eta \left[ \mathbf{n} \cdot \boldsymbol{\Sigma} \cdot \mathbf{n} - P + p + m(\ln \phi_f + \phi_s + \chi \phi_s^2) \right], \tag{38}$$

$$\mathbf{t} \cdot (\mathbf{V} - \mathbf{v}_s) = \beta \mathbf{n} \cdot \boldsymbol{\Sigma} \cdot \mathbf{t}. \tag{39}$$

The far-field velocity $V_0$ serves as a BC for the external Stokes flow (Eq. 35).

It is worthwhile to ponder a scheme of tuning the parameters to recover the diffusion-only and convection-only limits. In those limits, we should reproduce respectively the solutions for quiescent swelling [10, 19] and for flow through hydrogels [42, 43]. This is one way to demonstrate how our model unifies the two aspects that have been previously studied separately. Toward the diffusion-only limit, we need only reduce $V_0$ toward 0. Toward the convection-only limit, we need two conditions: $m \to 0$ and $\Delta \to 0$. The first removes the impetus for diffusion across the interface. The second puts the Fickian flux $\mathbf{j}_f$ of Eq. (5) to zero even though a gradient $\nabla \phi_f$ may arise from flow-induced gel compression. As $m$ is independent of $\Delta$, the Péclet number $V_0/\Delta$ will not serve as a single "dial" that could push our solution toward either of the two limits.

# 3   Results and discussion

The main objective of this paper is to present our new and unified model. The three examples of this section serve to validate the model against previous solutions in limiting cases, and to illustrate interesting solutions inaccessible to previous models.

## 3.1   Swelling and flow compression of hydrogel layer

Figure 1 shows a gel layer of initial thickness $L_0$ under the simultaneous action of two antagonistic mechanisms: compression by a uniform flow of velocity $V_0$ perpendicular to the gel surface, and swelling due to an abruptly imposed chemical potential jump across the interface. One can imagine this as the result of a change in ambient temperature. Because of the small spatial dimensions of microfluidic chips that employ hydrogels, the thermal equilibration occurs on a time scale much shorter than that for gel swelling. Thus, for simplicity, one typically imposes an abrupt and spatially uniform change in ambient condition [10, 29]. The right side of the gel is held fixed by a rigid but permeable mesh so that no displacement of the gel skeleton is allowed: $\mathbf{u}_s = 0$. In such a 1D
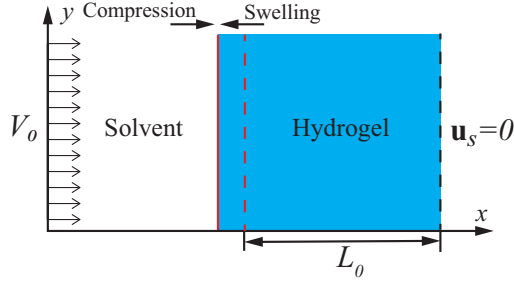
Figure 1: The setup for a hydrogel layer undergoing simultaneous flow-induced compression and thermodynamically-induced swelling.

Table 1: Five dimensionless model parameters for the swelling of a gel layer in a quiescent solvent, estimated in Appendix C.

| $\lambda_s$ | $\chi$ | $m$ | $\Delta$ | $\phi_{f0}$ |
|---|---|---|---|---|
| 1.94 | 0.2 | 8.0 | 17.2 | 0.01 |

setup, no flow, deformation, or spatial variation occurs along the $y$- or $z$-direction. By simplifying the governing equations (Eqs. 29–33) and boundary conditions (Eqs. 36–38) into their 1D form, the system can be solved by the finite-difference method, with the interface being tracked by Lagrangian mesh points. Details are given in Appendix B. In the absence of flow, the 1D swelling of hydrogel in a quiescent solvent has been studied by Hong *et al.* [19] and Yoon *et al.* [64]. More recently, Xu *et al.* [43,45] have obtained the solution for flow-compression without solvent diffusion or swelling. The current model accounts for both convection and diffusion of the solvent, and recovers the two limiting cases under suitable conditions.

### 3.1.1 Swelling without external flow

We first consider the limiting case of quiescent swelling without external flow ($V_0 = 0$). This is mostly because Yoon *et al.* [64] have reported experimental data for the process, which we can use to benchmark our model. Even in this limit, our model differs from previous models [19, 64] in our new boundary condition (Eq. 38). Thus, the diffusion limit provides a simplified setting for exploring the role of the interfacial penetration $\eta$ in the swelling of the gel.

We adopt the geometric setup of Yoon *et al.*'s experiment, with a planar gel layer attached to an impermeable solid substrate on one face, and exposed to a solvent on the other face (Fig. 1, except that the right boundary of the gel layer is now impermeable). The substrate prohibits displacement in its plane, and only allows swelling normal to the gel layer. Of the 9 dimensionless groups, $V_0 = 0$ for lack of an external flow, and $K$ also vanishes. Besides, the tangential slip coefficient $\beta$ does not appear in the current setup. Of the remaining 6 dimensionless parameters, 5 can be evaluated based on experimental evidence [64] (Table 1 and Appendix C). The only remaining parameter is the interfacial penetration $\eta$. It is new to our model and has never been reported experimentally before. Thus, it will be treated as a free parameter in fitting experimental data.

The interfacial penetration $\eta$ governs the ease with which the solvent crosses the interface of hydrogel, and is thus important to the swelling kinetics. Figure 2 depicts the displacement of the gel surface $u_{s1}$ as a function of time for three $\eta$ values. As expected, higher $\eta$ values correspond to faster swelling, owing to enhanced solvent infiltration.
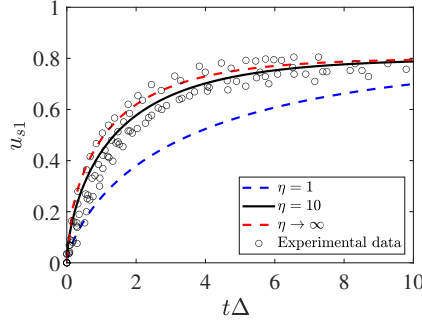
Figure 2: Model predictions of the evolution of the interfacial displacement $u_{s1}$ for a gel layer swelling in a quiescent solvent, for three $\eta$ values, and comparison with experimental data from Yoon *et al.* [64].

However, the effect quickly saturates; the swelling curve for $\eta = 10$ is already rather close to the asymptotic limit of $\eta \to \infty$.

We also compare our $u_{s1}$ with Yoon *et al.*'s experimental data gathered from gel layers of several initial thicknesses. To normalize their results for various gel thicknesses, Yoon *et al.* scaled time $t$ in a way that is equivalent to rescaling our dimensionless time as $t\Delta$ in our notation. Our model prediction at $\eta = 10$ runs through the band of the experimental data, offering a satisfactory fit given the degree of scatter in the data. The value $\eta = 10$, according to earlier estimations [68], is representative of the low-porosity hydrogels in the experiment. Therefore, in the limit of no external flow, our model captures the swelling dynamics of a gel layer in a quiescent solvent. Note, however, that the data are also reasonably well fitted by the curve for $\eta \to \infty$. In fact, Drozdov *et al.* [66] have previously fitted Yoon *et al.*'s data using the BC of Eq. (24) based on continuity of the chemical potential. This suggests that after the initial moment, the swelling behavior quickly becomes insensitive to the interfacial resistance to solvent penetration represented by a finite $\eta$. The latter effect must be sought in the initial fast kinetics of swelling, where Eq. (24) would have encountered a singularity.

The swelling process can also be appreciated from the temporal evolution of the $\phi_f(x)$ profiles in Fig. 3, for $\eta = 1$ and $\eta = 10$. The horizontal dashed line indicates the low porosity at the start of the simulation. Upon contact with the external solvent, the jump in chemical potential across the interface immediately pumps the solvent into the gel, via the boundary condition of Eq. (38) to raise the porosity inside the gel layer, while the gel expands simultaneously (see the $t = 0.001$ profile in panel a). In time, the high porosity extends further into the depth of the gel layer, as $\phi_f(x)$ approaches a uniform steady-state profile, $\phi_{f\infty} = 0.44$ for the current parameters. This value is determined by balancing the solid stress and the interfacial jump of the chemical potential, $\phi_s\sigma_s + m(\ln\phi_f + \phi_s + \chi\phi_s^2) = 0$, based on Eqs. (37, 38). At a larger $\eta$, the interfacial equilibration occurs more quickly (Fig. 3b). But the diffusion into the bulk of the gel takes time. The equilibrium porosity $\phi_{f\infty}$ does not depend on $\eta$.

Even in this "pure diffusion" limit, both terms of the generalized Maxwell-Stefan equation (Eq. 11) are at work. As the solvent enters the gel, it expands the polymer network and creates an inhomogeneous solid stress field $\boldsymbol{\sigma}_s$, and consequently a gradient in the (osmotic) pressure $p$ via the force balance of Eq. (32). The gradient of this pressure and the gradient of the chemical potential both contribute to the solvent flux, via the generalized Maxwell-Stefan equation. In principle, therefore, one may identify a convective part and a diffusive part in the solvent flux. This division will be further
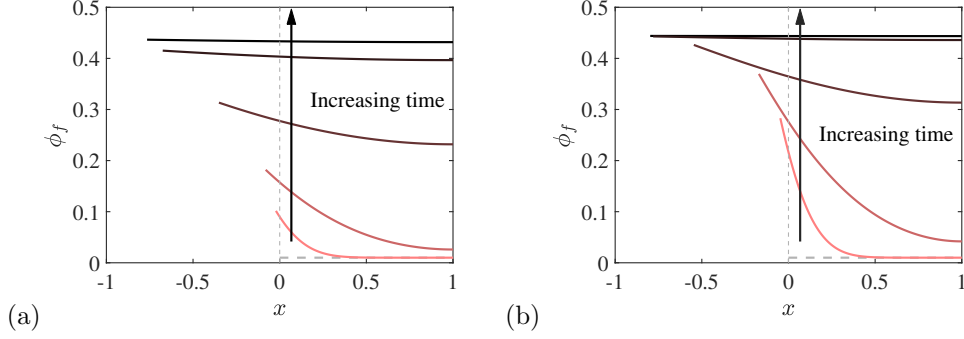
Figure 3: The evolving porosity profile with (a) $\eta = 1$, and (b) $\eta = 10$, plotted at different times: $t = 0.001, 0.01, 0.1, 0.5, 1$. The vertical grey dashed line marks the initial location of the interface, and the horizontal dashed line the initial $\phi_f$ profile.
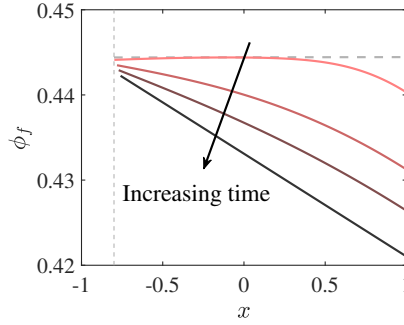


Figure 4: The porosity profiles of a swollen hydrogel compressed by a uniform flow at $t = 0.01, 0.1, 0.2$ and $1$ (from pink to black lines) with $V_0 = 0.2$ and $\eta = 1$. The vertical dotted line marks the upstream surface of the swollen gel before the external flow starts ($t = 0$), and the horizontal dashed line indicates the uniform porosity at $t = 0$.

explored in the following subsection.

### 3.1.2 Compression by external flow

After the hydrogel swells to its equilibrium state, we turn on the external normal flow of Fig. 1, and explore the interplay between the flow and the swollen hydrogel. The temporal evolution of the porosity profile is shown in Fig. 4. The normal flow compresses the hydrogel, and the compression initiates from the downstream boundary ($x = 1$) and is the most severe there. This is because the Darcy drag accumulates downstream and the downstream interface is fixed ($\mathbf{u}_s = 0$). Eventually, the system reaches a steady state at $t \approx 1$, indicated by the black line in Fig. 4, with the porosity $\phi_f$ decreasing monotonically downstream. This behavior closely resembles our previous simulations of 1D compression without the swelling effect [42, 43]. However, a major distinction is that in the current unified model, the chemical potential gradient drives a diffusion flux, which is absent from the earlier studies. Moreover, the chemical potential modifies the pressure jump across the boundary via Eq. (38). As a result, the pressure $p$ inside the hydrogel may be higher than the external solvent pressure $P$ thanks to the jump in chemical potential. This contrasts the purely hydrodynamic scenario [42, 43], where $P$ must exceed $p$ to drive the solvent into the hydrogel.
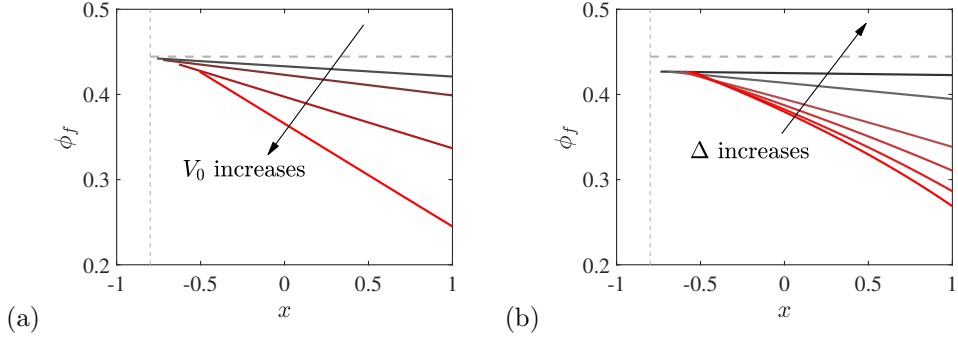
Figure 5: (a) The steady-state porosity profiles for a series of $V_0$ values (0.05, 0.2, 0.4, 1, 2) and a fixed $\Delta = 17.2$; (b) The steady-state profiles for different $\Delta$ values (0.25, 0.5, 1, 2, 10, 100) and a fixed $V_0 = 0.2$.

The competition between solvent convection and diffusion can be probed by a parametric study. With increasing $V_0$, Fig. 5(a) shows progressively more severe compression of the gel layer, with the greatest reduction in $\phi_f$ at the immobile downstream boundary $x = 1$. Conversely, increasing the diffusivity $\Delta$ results in less compression and a more uniform porosity profile $\phi_f$ (Fig. 5b), as can be expected from the diffusive flux of Eq. (5). Interestingly, even in the limit of $\Delta \to \infty$, the flat $\phi(x)$ profile is still below the initial profile. This is because the external flow produces an interfacial pressure drop according to our boundary condition in Eq. (38). This pressure drop in turn causes an interfacial compression, visible in the $t = 0.01$ profile of Fig. 4, that is inversely proportional to the interfacial penetration $\eta$ [43]. This effect cannot be compensated for by strong diffusion, and as a result, the Péclet number $Pe = V_0/\Delta$ is of limited utility in the current context.

In steady state ($v_s = 0$), we can separate the solvent flux explicitly into a convective and a diffusive component. Using the generalized Maxwell-Stefan equation (Eq. 31) and the solvent continuity across the interface (Eq. 36), we write $V_0$ as the sum of a diffusive flux $V_d$ and a convective $V_c$:

$$V_0 = \phi_f v_f = -\Delta(1 - 2\chi\phi_f)\frac{\partial \phi_f}{\partial x} - \frac{\phi_f}{\phi_s}\frac{\partial p}{\partial x} = V_d + V_c. \tag{40}$$

Even for a fixed $V_0$, its two parts $V_d$ and $V_c$ vary through the depth of the gel layer, their relative importance being controlled by the porosity $\phi_f$. A high porosity, at light compression, favors $V_c$ whereas severe compression favors $V_d$.

Figure 6 plots the steady-state profiles of $V_d/V_0$ for a range of $V_0$ and $\Delta$ values. As $V_d/V_0 + V_c/V_0 = 1$, the vertical distance from the curve up to the gray dashed line at 1 represents the fraction of the convective flux $V_c/V_0$. At the fixed $\Delta = 17.2$, $V_d$ is dominant as diffusion accounts for more than 85% of the solvent flux (Fig. 6a). For each of the $V_0$ values, $V_d$ increases with $x$. This is because the porosity $\phi_f$ declines downstream (Fig. 5a), and as a result $V_d$ becomes more important relative to $V_c$ according to Eq. (40). Perhaps surprisingly, Fig. 6(a) shows that a stronger external flow $V_0$ raises the proportion of diffusion relative to convection. This is similarly because $V_0$ compresses the gel layer to reduce $\phi_f$. Another interesting feature is that the curve becomes flat for small $V_0$, implying a constant $V_d/V_c$ ratio throughout the gel. The overall momentum balance (Eq. 32) implies $\partial p/\partial x \propto \partial \phi_f/\partial x$ in this 1D case, as the solid stress $\sigma_s$ is a function of the local strain, which in turn depends on $\phi_f$ only. A vanishing $V_0$ causes weak compression and a nearly constant $\phi_f(x)$, and thus a nearly constant $V_d/V_c$ ratio.
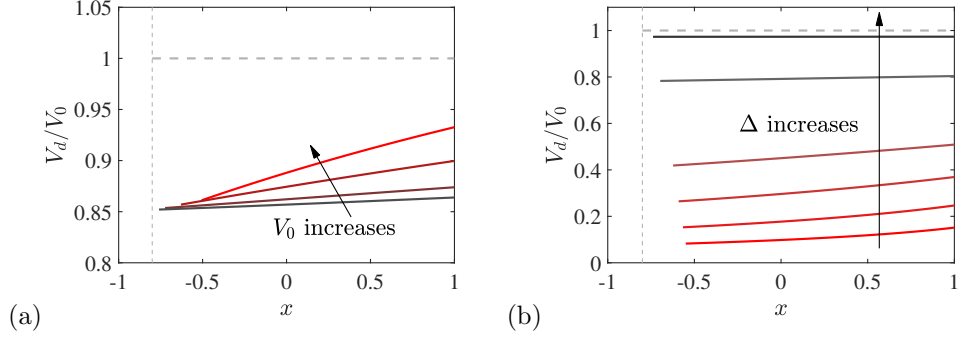
Figure 6: The steady-state profiles of the relative diffusive flux $V_d/V_0$ for (a) increasing $V_0$ values ($V_0 = 0.05, 0.2, 0.4, 1, 2$) and a fixed $\Delta = 17.2$; (b) increasing $\Delta$ values ($\Delta = 0.25, 0.5, 1, 2, 10, 100$) and a fixed $V_0 = 0.2$.

On the other hand, if we keep $V_0$ constant and increase $\Delta$ (Fig. 6b), the proportion of diffusion flux increases continuously toward 1, implying domination by diffusion, as one may expect. Note that in Fig. 6, $V_0$ and $\Delta$ have similar effects in favoring the diffusive flux over the convective one. Thus, a naive application of the Péclet number $Pe = V_0/\Delta$ would not be appropriate in this analysis.

To sum up this section, the swelling of a gel layer in a quiescent solvent bath can be accurately captured by our unified model. Even in the absence of external flow, a convective flux acts alongside a diffusive one. If an external flow is imposed, the relative importance of the two mechanisms are controlled by the dimensionless parameters $V_0$ and $\Delta$. Because of the complication of gel compression that varies spatially inside the gel, the interplay between solvent convection and diffusion cannot be encapsulated by a Péclet number.

## 3.2   Dynamics of a spherical shell of hydrogel

Another well-studied problem is the swelling and deswelling of a gel sphere [10, 20, 25, 31, 32]. In the following, we consider the somewhat more complex geometry of a spherical shell of hydrogel (called the "gel shell" hereafter; Fig. 7). This is motivated by recent experiments that aimed to manufacture capsules from hydrogels [69, 70]. But our immediate goal is to use this problem to demonstrate the coupling between solvent diffusion and convection in a curvilinear geometry.

We first consider the swelling of a gel shell after a sudden change in ambient condition in a quiescent solvent bath. Then we study the simultaneous action of a sudden ambient change and an expanding gas bubble at the center, which may arise from chemical reaction [69, 70] or nucleation following a temperature change. The first is a "pure diffusion" process, whereas the second couples convection and diffusion. In this section, the following parameters are fixed: $\lambda_s = 1.94$, $\eta = 10$, $\Delta = 1$ and $\chi = 0.2$. The parameter $\Delta = 1$ is chosen to allow an evenly matched competition between diffusion and convection.

### 3.2.1   Swelling of a spherical shell in quiescent bath

In keeping with convention [19], the dry-polymer state is taken to be the reference state of zero solid stress. The dry shell has an outer radius twice its inner radius, and the dry shell thickness $L_0$ is used as the characteristic length. Put into contact with a solvent at $m = 4$, the shell swells initially to reach chemical and mechanical equilibrium with the
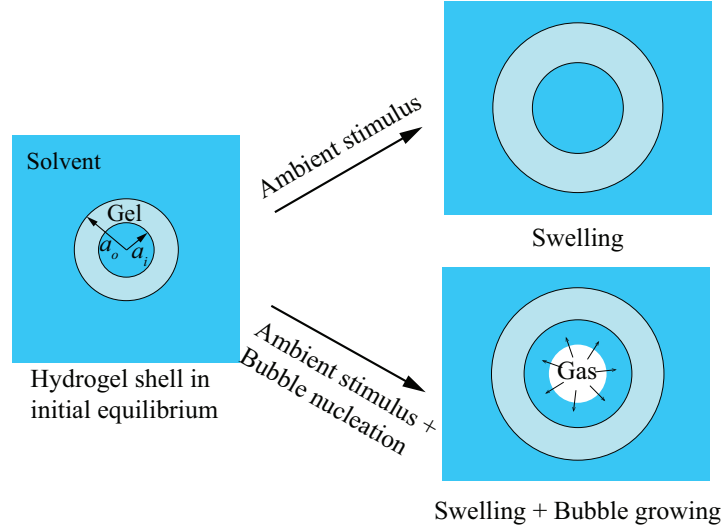
Figure 7: Deformation of a spherical shell of hydrogel driven by swelling due to an ambient stimulus, or by the simultaneous action of the ambient stimulus and an expanding bubble inside the shell.

solvent inside and outside, with an initial inner radius $a_i = 1.19$, outer radius $a_o = 2.38$ and uniform porosity $\phi_{f0} = 0.408$. This initial equilibrium state is determined by balancing the osmotic pressure $p$ with the chemical potential on the one hand (Eq. 38), and with the elastic tensile stress in the swollen network on the other (Eq. 37). Now we impose a sudden change of $m$ from 4 to 6. This disrupts the chemical balance so the solvent diffuses into the shell from both the inside and the outside surface. There is no external flow, so $V_0 = 0$. Similar to the planar gel layer of Section 3.1, the 1D swelling of the gel shell is solved by finite difference. See Appendix B for details.

Starting from the initial condition specified above, our model predicts the subsequent swelling of the shell in the quiescent solvent bath, eventually approaching a new chemical and mechanical equilibrium. Figure 8(a) illustrates this process via the porosity $\phi_f(r)$ profiles. As time progresses, the color of the lines darkens from pink to black. For ease of description, we divide the whole process roughly into three stages: (i) interfacial swelling (blue arrows), (ii) bulk swelling (red arrows), and (iii) solvent transportation from outside the shell to inside (green arrows).

In the first stage, both surfaces of the gel absorbs solvent to raise the local osmotic pressure, driven by the BC of Eq. (26). Toward the end of stage (i), the gel approaches the interfacial balance represented by Eq. (24). At the relatively large interfacial penetration $\eta = 10$, the interfacial swelling occurs quickly, and is nearly complete by $t = 0.01$; see the first pink profile in Fig. 8(a).

In the second stage, roughly from $t \approx 0.01$ to $0.2$, the interfacial regions swollen in the first stage at both surfaces widen and spread toward the interior of the gel shell. The interfacial swelling has produced higher pressure and chemical potential locally, and both the pressure and the chemical potential gradients drive the solvent transport into the interior of the gel. This raises the porosity in the interior of the shell to yield a relatively flat $\phi_f(r)$ profile at the end of stage (ii). The swelling of the bulk pushes the outer surface outward and the inner surface inward, further shrinking the inner radius $a_i$ in stage (ii) (Fig. 8b). Owing to the spherical geometry of the shell, the decrease in $a_i$ incurs a tangential compression of the gel at the inner surface, which for a time reduces the local $\phi_f$, indicated by the small red arrow in Fig. 8(a). The end of stage (ii)
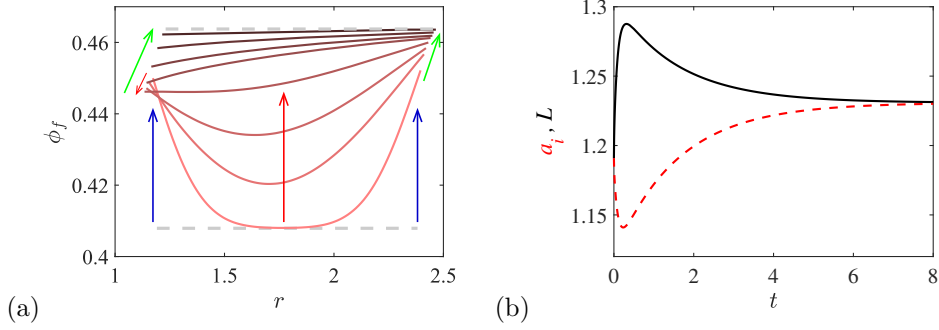
Figure 8: Swelling of the gel shell. (a) Temporal evolution of the $\phi_f(r)$ profile, with darkening colors indicating time progression: $t = 0.01, 0.05, 0.1, 0.2, 0.5, 1, 2, 4$. The blue, red and green arrows mark the 3 stages of swelling. The initial state is indicated by the lower horizontal grey dashed line, while the final equilibrium by the upper one. (b) Non-monotonic evolution of the thickness of the hydrogel shell $L$ (black line) and the inner radius $a_i$ (red dashed line).

corresponds roughly to the $\phi_f(r)$ profile becoming flat at the inner surface.

At the start of stage (iii), the inner surface experiences an inversion in the gradient $\partial \phi_f / \partial r$ so that the $\phi_f(r)$ profile assumes a uniformly positive gradient; see the $t = 0.5$ curve in Fig. 8(a). Stage (iii) is thus dominated by a solvent flux from the outside to the inside of the shell, driven by the gradients of pressure $p$ and chemical potential $\mu_m$. As a result, the inner radius $a_i$ starts to increase, and this trend persists throughout stage (iii). The thickness of the shell $L$ increases until $t = 0.32$, when the exuding flux at the inner surface equals the absorbing one at the outer surface and $L$ peaks at $L_{max} = 1.29$ (Fig. 8b). As both the $p$ and $\mu_m$ gradients subside in time, $\phi_f$ becomes more uniform in space. In the end, $\phi_f(r)$ approaches a uniform equilibrium profile dictated by a new chemical and mechanical balance. In this equilibrium, the gel swelling has to be spatially uniform. Thus, the shell maintains the same spatial proportion as in the initial state, and indeed as in its dry state. In particular, $L = a_i$, even though the shell thickness and inner radius are both greater than in the initial state.

In swelling of the planar gel layer (Fig. 3) and the gel shell (Fig. 8), the "diffusive flux" driven by the gradient $\nabla \phi_f$ and the "convective flux" driven by the gradient $\nabla p$ often seem to act in concert. In particular, Eq. (40) shows the diffusive and convective fluxes to be proportional to each other under weak flow compression of a planar gel layer. Such proportionality and synchronization may have contributed to the common practice of writing the total flux either as Fick's law [19] or as Darcy's law [10] in 1D quiescent swelling. For the gel shell, the curved geometry complicates the situation as non-zero strains arise in both the radial and azimuthal directions. Such 2D strains disrupt the proportionality between $\nabla p$ and $\nabla \phi_f$. Consequently, the diffusive and convective fluxes no longer synchronize perfectly (Fig. 9), with the diffusive flux $V_d$ following the variation of the convective flux $V_c$ with a slight delay.

### 3.2.2 Deformation of a spherical shell driven by a gas bubble

We now consider the dynamics of the gel shell subject to the simultaneous action of two processes: the swelling studied in the above, triggered by a sudden environmental stimulus, and the nucleation and growth of a gas bubble in the center of the shell, which may be triggered by the same stimulus (Fig. 7). The expanding bubble drives a radially outward flow of the solvent, thus setting up a situation where solvent diffusion and
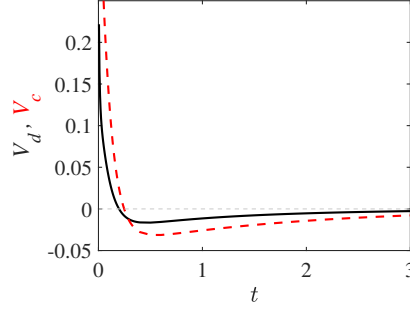
Figure 9: Temporal evolution of the diffusive flux $V_d$ (solid line) and the convective flux $V_c$ (red dashed line) at the inner surface.
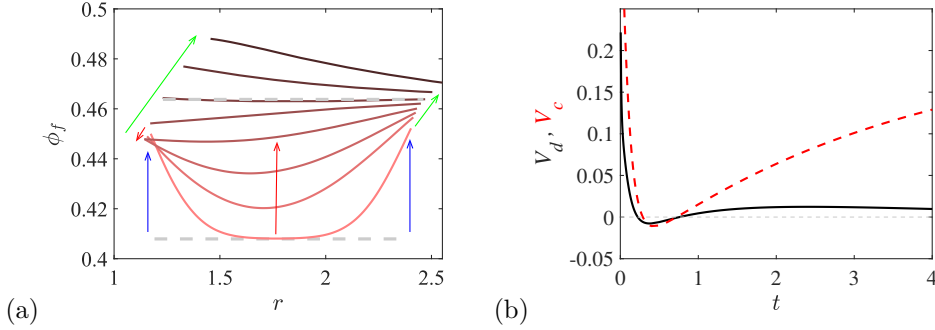


(a)

(b)

Figure 10: Dynamics of the gel shell driven by swelling and an expanding bubble. (a) Temporal evolution of the $\phi_f(r)$ profile, with darkening colors marking time progression: $t = 0.01, 0.05, 0.1, 0.2, 0.5, 1, 2, 4$, and the blue, red and green arrows indicating the 3 stages of gel deformation. (b) Temporal evolution of the diffusive flux $V_d$ (solid line) and the convective flux $V_c$ (red dashed line) at the inner surface.

externally driven convection coexist.

According to the classical Epstein-Plesset model for diffusion-driven bubble growth, the bubble radius changes in time as $r_g = A\sqrt{t}$, where the material constant $A$ is determined by the gas concentration and diffusivity in the liquid and gas density inside the bubble [71,72]. This affects the gel shell by imposing a radial solvent velocity at its inner surface (of radius $a_i$):

$$V = \frac{A^3}{2a_i^2}\sqrt{t}, \tag{41}$$

which enters the boundary conditions of Eqs. (36) and (38). Since $V$ changes in time, it is awkward to define a "far-field" velocity scale $V_0$ in this case. The dimensionless $V$ serves in its place, with the constant $A$ assigned a moderate value of $\sqrt[3]{2/5} \approx 0.737$. Besides, the viscous normal stress $\Sigma$ of the solvent flow is negligible in comparison to the Darcy drag inside the gel. Thus we set $K = 0$ in Eq. (35) and omit $\Sigma$ from the BCs of Eqs. (37) and (38). All the other dimensionless parameters are the same as in the preceding subsection.

The expansion of the gel shell is depicted in Fig. 10. Similar to the quiescent swelling of the previous subsection, the temporal evolution of the $\phi(r)$ profile also exhibits three stages, indicated by the blue, red and green arrows in Fig. 10(a). The first two stages resemble their counterparts in Fig. 8(a); the bubble expands slowly at the start (Eq. 41)

and has not yet imparted much effect on the gel. In the third stage, the bubble manifests itself in several distinct features of $\phi(r)$. First, the azimuthal stretching elevates $\phi_f$ quickly, especially at the inner surface of the shell, such that the previous equilibrium state of Fig. 8 (grey dashed horizontal line at $\phi_{f\infty} = 0.464$) is surpassed at $t = 1$. Second, later profiles for $t > 1$ assume a downward slope, with the porosity decreasing monotonically from the inner surface to the outer surface. This is reminiscent of the 1D compression of the planar gel layer (Fig. 5), where the cumulating Darcy drag produces more severe solid compression further downstream. As a consequence, the diffusive flux turns positive (radially outward) in the third stage (Fig. 10b). Finally, as the bubble continues to expand, so does the gel shell, causing a continual rise of $\phi_f$ as the gel is stretched. The shell thickness, not shown in Fig. 10, reaches a maximum of $L_{max} = 1.28$ at $t = 0.24$, comparable to Fig. 8(b), and then continues to decrease while the shell expands and stretches. We end the simulation at $t = 4$, when the bubble interface reaches the shell's inner surface, initiating complex gas-gel interactions beyond the scope of this study.

It is interesting to contrast the convection and diffusion velocities of Fig. 10(b) with their counterparts in the 1D planar geometry (Fig. 6a). In the spherical shell, the growing dominance of the convective flux $V_c$ in time is evidently due to the increasing velocity of the expanding bubble (Eq. 41). In contrast, increasing $V_0$ in Fig. 6(a) produces more severe compression of the 1D gel layer, thus elevating the $\phi_f$ gradient and favoring $V_d$ over $V_c$. One reason for this difference is that the planar gel layer is constrained by the solid substrate, whereas the gel shell is free to expand outward. Another is the azimuthal stress $\sigma_\theta$ in the shell geometry, which helps to counterbalance the Darcy drag and to relieve the $\phi_f$ gradient. Thus, in Fig. 10(b), the diffusive flux $V_d$ does not experience a substantial increase as $V_c$ does, underscoring how the curvilinear geometry may disrupt the coordination between $\nabla p$ and $\nabla \phi_f$. Such disruption has already been noted for the quiescent swelling of Fig. 9, albeit at a much reduced magnitude.

## 3.3 Flow around a gel cylinder

Going beyond the 1D planar and spherical geometries above, we now consider a 2D problem with flow around a gel cylinder. It is motivated by experiments that used a row of gel cylinders, placed abreast facing the flow, as pH-sensitive throttle values in a microfluidic device [11]. Assuming symmetry between neighboring cylinders, we adopt the computational domain of Fig. 11 with symmetry conditions on the top and bottom boundaries. As in the experiment, the gel forms a concentric "jacket" around a rigid post. A uniform flow of velocity $V_0$ enters the domain from the left, carrying high-pH fluids that causes the gel to expand.

In this example, the reference state for measuring the elastic strain and stress is not the dry-polymer state as used in the preceding examples and in the literature [19], but is a uniform gel at porosity $\phi_{f0} = 0.2$ and chemical potential $m = 0$ in equilibrium with the environment. This is because in the experiment [11], the gelation happens *in situ* by photopolymerization of a precursor solution. The solid constitutive equation (Eq. 33) is modified slightly by setting $J = (1 - \phi_{f0})/\phi_s$, in place of $J = 1/\phi_s$, in Eq. (16). To initiate the swelling, we impose a sudden and uniform change of the parameter $m$ from 0 to 4 throughout the gel at the start of the simulation. The initial outer radius of the hydrogel is taken as the characteristic length: $a_o|_{t=0} = 1$, and the radius of the inner solid cylinder is $a_i = 0.5$. The computation domain has a height $H = 2$ and a length of $3H$ (Fig. 11). A uniform velocity $V_0 = 0.5$ is imposed on the left boundary and a stress-free boundary condition applies on the right boundary. For such entry and exit BCs, channel flow computations normally require a longer length. But our poroelastic gel with a small $K = 0.01$ is insensitive to the external flow. Realistic values of $K \sim (r/L_0)^2$ are
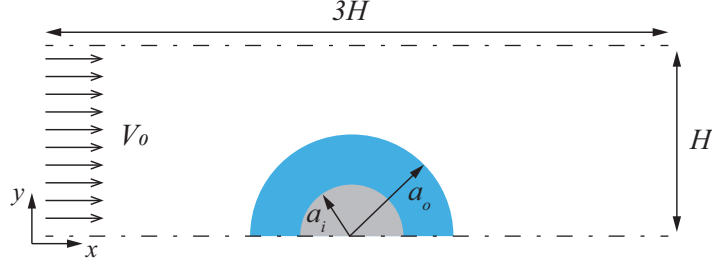
Figure 11: Computational setup of the flow around a gel cylinder. The grey area denotes the solid cylinder and the surrounding blue layer is the hydrogel. The flow with velocity $V_0$ goes from the left to the right, with symmetry conditions imposed on the top and bottom boundary.

likely to be even smaller. Numerical experimentation shows negligible changes to the gel displacement when the channel is lengthened. On the top and bottom boundaries, symmetry conditions prevail. At the surface of the solid cylinder, no displacement of the solid skeleton of the gel is allowed, and there is no fluid penetration. Since we adopt Darcy flow for the fluid, with no Brinkman stress, there is no need to specify the tangential fluid velocity. The governing equations are solved in the 2D domain by finite elements, with a fixed-mesh arbitrary Lagrangian-Eulerian method to track the moving gel surface. Algorithmic details can be found in Li *et al.* [42]. Mesh and time-step refinements have been carried out to ensure adequate spatial and temporal resolution. A typical grid has about 900 cells, each a quadrilateral Q3 element with 4 nodes per edge, and the finest mesh size $\Delta x \sim 0.008 a_0$. The time step is shortest $\Delta t = 10^{-6}$ at the start of the simulation, and increases to $10^{-4}$ after the initial rapid swelling.

A typical solution is depicted in Fig. 12. In the early times, the external flow field quickly establishes itself. But the most interesting feature is the rapid swelling of the gel, reflected by the interstitial fluid velocity $\mathbf{v}_f$ in Fig. 12(a). As the gel expands radially outward, the solvent is driven inward to fill the increasing porosity. Thus, the $\mathbf{v}_f$ field by itself does not satisfy volume conservation as expected for single-phase flows. At oncoming velocity $V_0 = 0.5$, the flow-induced gel deformation is weak at this stage, but $\mathbf{v}_f$ exhibits an asymmetry caused by the external flow. By $t = 2.45$, the solution approaches a steady state (Fig. 12b), the gel thickness having grown by roughly 30%. Because of the external flow, there remains a steady $\mathbf{v}_f$ inside the gel, indicated by the streamlines of Fig. 12(b). Consequently, $\phi_f$ and $\boldsymbol{\sigma}_s$ remain non-uniform in space, and a small diffusive flux persists as well.

To further examine the effect of the external flow in gel deformation, we plot in Fig. 13(a) the temporal evolution of the gel displacement at the upstream "stagnation point" (the red dot in Fig. 12b) and the downstream stagnation point (the blue dot). The upstream side of the gel is compressed by the flow, and its radial expansion is reduced relative to that without the flow (the dashed curve). In contrast, the downstream side of the gel experiences greater expansion due to the low pressure at the back of the cylinder. The top region of the cylinder has expanded upward by roughly the same amount as in quiescent swelling, while the flow sweeps the top downstream by about 0.1. Figure 13(b) shows the evolution of the $\phi_f$ profile along the $x$-axis, the coordinate $x_w$ being the distance to the wall of the solid cylinder. At the initial stage ($t = 0.058$), the profile is approximately symmetric between the upstream ($x_w < 0$) and downstream ($x_w > 0$) portions. This reflects the initial domination of swelling over the external flow. As the swelling weakens in time, the external flow manifests itself more clearly by compressing the upstream region of the gel while expanding its downstream region.
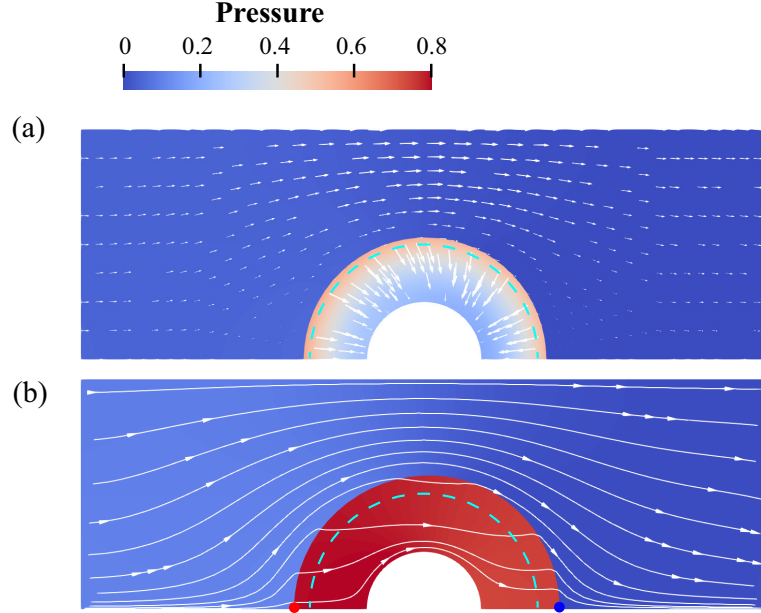
19

Figure 12: (a) The fluid velocity field shortly after the start of flow ($t = 0.058$). (b) Streamlines in the steady state ($t = 2.45$). In both plots, the dashed cyan line delineates the initial gel surface. The color of the graph represents the pressure. The red and blue dots mark the front and rear "stagnation points" where gel deformation will be compared. The material parameters are $\lambda_s = 1.94$, $\eta = 1$, $\beta = 1$, $\Delta = 1$, $K = 0.01$ and $\chi = 0.2$. The initial porosity $\phi_{f0} = 0.2$. At $t = 0$, the flow starts with $V_0 = 0.5$ and $m$ changes from 0 to 4.
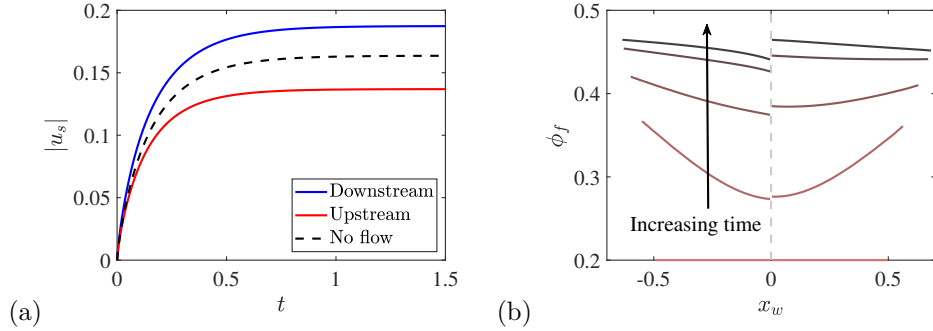


Figure 13: (a) Temporal evolution of the gel displacement at the upstream and downstream stagnation points marked by the red and blue dots in Fig. 12(b). The dashed curve represents the interfacial displacement without external flow. (b) Temporal evolution of the porosity profiles $\phi_f(x_w)$ along the center line $y = 0$, at different times $t = 0, 0.058, 0.18, 0.43$ and $2.45$ (essentially the steady state). The x-axis $x_w$ is the distance to the wall of the solid cylinder.

Thus, the $\phi_f$ profile becomes increasingly asymmetric, with lower porosity upstream than downstream.

# 4    Conclusion

We have formulated a poroelasticity model to explicitly integrate two modes of solvent transport through a hydrogel: convection driven by an external pressure gradient, and diffusion driven by the gradient of a chemical potential inside the hydrogel. To accomplish this seemingly straightforward goal, we have had to resolve two complications.

The first is the current usage of two parallel systems of nomenclature and formulation in modeling hydrogel swelling or deswelling in a quiescent solvent bath, one expressing the solvent flux as a diffusive Fickian flux, and the other as a convective Darcian flux. The ambiguity seems to stem from inconsistent definitions for the chemical potential $\mu_m$ and the osmotic pressure $\Pi$. Between certain models, the same entity has been called by one or the other name [10,19]. While the chemical-potential gradient $\nabla \mu_m$ fits naturally in the framework of Fickian diffusion, the pressure gradient $\nabla \Pi$ evokes Darcy's law. Fortunately, the algebraic similarity between Fick's law and Darcy's law has enabled both formalisms to produce essentially the same predictions. Therefore, insofar as the diffusivity and permeability are treated as phenomenological constants, the two systems differ in notations but not in substance when applied to quiescent swelling problems. In our integrated model, however, we have to clearly distinguish the two modes of solvent transport, and use Fick's law or Darcy's law accordingly. Algebraically, this is facilitated by combining the osmotic pressure and the hydrodynamic pressure into a single Lagrange multiplier $p$.

The second issue is more substantive. In its standard formulation, Fick's law is expressed as fluxes relative to an average velocity, and this average velocity is ambiguous if an externally driven flow passes through a hydrogel. Our solution to this problem is to generalize the Maxwell-Stefan form of the diffusive flux, so as to obviate the need for an average velocity. Thus, the solvent flux is expressed as the sum of a diffusive flux $V_d \propto (-\nabla \mu_m)$ and a convective flux $V_c \propto (-\nabla p)$. This forms the basis for our unified model.

Another key feature of our model is a penetration boundary condition, derived from the requirement of positive entropy production on the gel-solvent interface. Thus, in place of previous assumption of instantaneous interfacial equilibration, our boundary condition stipulates a normal solvent flux proportional to the interfacial imbalance between the jumps in normal stress and in chemical potential. This remedies a singularity suffered by the previous boundary condition: upon abrupt change of an ambient condition, the gel must deform instantaneously to develop a finite strain and stress.

Applied to 1D and 2D calculations, our model reveals interesting scenarios where the diffusive and convective modes of solvent transport interact to yield novel physical outcomes. The main results can be summarized as follows:

(a) The model is capable of describing swelling experiments of a planar layer of hydrogel submerged in a quiescent solvent bath. This is no surprise, as the unified model encompasses quiescent swelling as a component.

(b) Even in this "diffusion-only" limit, the (osmotic) pressure gradient induces a "convective flux" $V_c$, which reinforces the diffusive flux $V_d$ in the 1D planar geometry.

(c) In the curvilinear geometry of a spherical shell of hydrogel, the swelling exhibits distinct stages dominated by different physical mechanisms, with non-monotonic changes in the shell thickness and inner radius.

(d) Interesting interaction between $V_c$ and $V_d$ arises in curvilinear and two-dimensional geometries, where multiple strain components may compress or extend the local solid network. During the swelling of the spherical shell, for example, $V_c$ and $V_d$

are no longer synchronized as they are in planar 1D geometry with a single strain component.

(e) When an external flow is imposed on a swelling hydrogel, it directly affects the convective flux $V_c$ in the gel and the coupling between $V_c$ and $V_d$. This coupling depends on the geometry of the problem, and is not well represented by a Péclet number in general.

(f) The 2D flow around a gel cylinder demonstrates the potential of the model in multi-dimensional applications.

The flow problems presented here are relatively simple, and serve to illustrate the capability of the unified model to describe physical processes that involve simultaneous actions of solvent convection and diffusion. Nevertheless, this work offers a theoretical framework and numerical tool for simulating and analyzing a class of emerging technological problems, e.g., the function of gel-based microfluidic actuators, the wet-spinning of fibers by passing and stretching hydrogel filaments in a coagulant bath, and the design of gel-based lab-on-chip devices.

# Acknowledgements

# Appendix A    Interfacial boundary conditions

In this Appendix, we temporarily revert to the use of dimensional variables in discussing the boundary conditions. The boundary conditions of Eqs. (21, 22) correspond to the so-called BC2 derived by Young *et al.* [41, 43], but differ somewhat in notations. In its original form, BC2 consists of the following three boundary conditions [41, 43]:

$$(\mathbf{V} - \mathbf{v}_f) \cdot \mathbf{n} = \eta \, \mathbf{n} \cdot \left[ (\mathbf{\Sigma} - P\mathbf{I}) - (\boldsymbol{\sigma}_s - p\mathbf{I}) \right] \cdot \mathbf{n}, \tag{A.1}$$

$$(\mathbf{V} - \mathbf{v}_f) \cdot \mathbf{t} = \beta \, \mathbf{n} \cdot \mathbf{\Sigma} \cdot \mathbf{t}, \tag{A.2}$$

$$\phi_s \left( \mathbf{v}_s - \mathbf{v}_f \right) \cdot \mathbf{t} = -\beta \, \mathbf{n} \cdot \boldsymbol{\sigma}_s \cdot \mathbf{t}. \tag{A.3}$$

Using the interfacial fluid continuity and traction balance (Eqs. 19, 20), we transform Eq. (A.1) to

$$(\mathbf{V} - \mathbf{v}_s) \cdot \mathbf{n} = \eta \left( \phi_f / \phi_s \right)^2 \left( \mathbf{n} \cdot \mathbf{\Sigma} \cdot \mathbf{n} - P + p \right). \tag{A.4}$$

As we only consider Darcy flows in the current work, we no longer need a BC on the tangential $\mathbf{v}_f \cdot \mathbf{t}$. Eliminating $\mathbf{v}_f$ from Eqs. (A.2, A.3), Xu *et al.* [43] showed that in Darcy flows, the two tangential BCs should be replaced by

$$(\mathbf{V} - \mathbf{v}_s) \cdot \mathbf{t} = \beta \left( 1 + \phi_s^{-2} \right) \mathbf{n} \cdot \mathbf{\Sigma} \cdot \mathbf{t}. \tag{A.5}$$

Equations (A.4, A.5) are the basis for the boundary conditions of Eqs. (21, 22).

Furthermore, there are two notational changes in the definition of $\eta$ and $\beta$. First, we add the solvent viscosity $\mu$ on the left hand side of Eq. (A.4). This reflects the

expectation that the stresses inside and outside the gel vary linearly with $\mu$. In the current form, therefore, $\eta$ no longer depends on $\mu$. It has the dimension of length and depends solely on the geometric features of the interface. Similarly, $\mu$ is added to the left hand side of Eq. (A.5) to make $\beta$ a length. Our penetration length $\eta$ and slip length $\beta$ can be likened, respectively, to the "transpiration length" and the Navier slip length [73]. Second, the factor $(\phi_f/\phi_s)^2$ in Eq. (A.4) is now absorbed into $\eta$ to simplify the notation, giving rise to Eq. (21). Similarly, we absorb $(1 + \phi_s^{-2})$ into $\beta$ in Eq. (A.5) to arrive at Eq. (22). In principle, $\eta$ and $\beta$ are functions of $\phi_f$, and Feng and Young [41] have explored their limits at $\phi_f \to 0$ and $\phi_f \to 1$. Their general function forms require a detailed pore-scale study [68]. In this paper, we take $\eta$ and $\beta$ to be constants in Eqs. (21, 22) for simplicity.

To extend Eq. (21) to account for solvent diffusion across the interface, we start by considering the diffusion-only limit without convection. Following Hong *et al.* [19], we require that the total free energy not increase in time during the diffusion, and as sufficient conditions, that neither the elastic energy nor the mixing energy increase in time. As the gel domain deforms in time, it is convenient to write the volume integral of the mixing energy in the time-invariant Lagrangian frame, indicated by a hat ˆ:

$$\frac{d}{dt} \int_{\hat{\Omega}} W_m \, d\hat{V} = \int_{\hat{\Omega}} \frac{\partial W_m}{\partial C} \frac{dC}{dt} \, d\hat{V} = \int_{\hat{\Omega}} \mu_m (-\hat{\nabla} \cdot \hat{\mathbf{j}}_i) \, d\hat{V} \le 0, \qquad (A.6)$$

where $\hat{\Omega}$ is the domain of the gel, and the number flux of the solvent $\hat{\mathbf{j}}_i$ is related to $C$ by $dC/dt + \hat{\nabla} \cdot \hat{\mathbf{j}}_i = 0$. Applying the divergence theorem and transforming back to the Eulerian frame (without the hat ˆ), we have:

$$\int_{\hat{\Omega}} \hat{\nabla} \mu_m \cdot \hat{\mathbf{j}}_i \, d\hat{V} - \int_{\hat{\Gamma}} (\hat{\mathbf{n}} \cdot \hat{\mathbf{j}}_i) \mu_m \, d\hat{A} = \int_{\Omega} \nabla \mu_m \cdot \mathbf{j}_i \, dV - \int_{\Gamma} (\mathbf{n} \cdot \mathbf{j}_i) \mu_m \, dA \le 0, \qquad (A.7)$$

where $\Gamma$ is the surface of the gel domain $\Omega$, and the transformation to the Eulerian frame is based on $d\hat{V} = J \, dV$ and Eqs. (27–29) of Hong *et al.* [19]. Fick's law (Eq. 3) ensures that the volume integral on the right-hand-side be non-positive. Linking $\mathbf{j}_i$ to the relative velocity $\mathbf{v}_f - \mathbf{v}_s$ via Eq. (8), we propose a new BC such that the surface integral stays non-negative:

$$\mathbf{n} \cdot (\mathbf{v}_f - \mathbf{v}_s) = \alpha \mu_m, \qquad (A.8)$$

where the positive coefficient $\alpha$ represents a kind of interfacial permeability, i.e., the ease with which the interfacial jump in chemical potential $\mu_m$ drives the solvent across the gel interface. Note that by definition (Eq. 2), $\mu_m = 0$ in the solvent bath ($\phi_f = 1$).

In the general case, the total solvent flux across the interface $\Gamma$ is the sum of a convective and a diffusive component. This suggests combining Eqs. (21) and (A.8) additively. Again using the solvent continuity of Eq. (19), we arrive at Eq. (23):

$$\mu \left( \mathbf{V} - \mathbf{v}_s \right) \cdot \mathbf{n} = \eta \left( \mathbf{n} \cdot \boldsymbol{\Sigma} \cdot \mathbf{n} - P + p + \frac{\mu_m}{v} \right), \qquad (A.9)$$

which amounts to choosing $\alpha = \eta/(\mu v \phi_f)$. This is partly for dimensional uniformity. More importantly, having $\mu_m/v$ added to the pressure $p$ maintains consistency with existing formalisms for the diffusion-only limit (cf. Eq. 18 of Hong *et al.* [19]).

# Appendix B    One-dimensional solutions

In the planar 1D geometry of the gel layer of Section 3.1, we simplify the dimensionless governing equations into the following form:

$$\frac{\partial \phi_f}{\partial t} + \frac{\partial (v_f \phi_f)}{\partial x} = 0, \tag{B.1}$$

$$v_f \phi_f + v_s \phi_s = V_0, \tag{B.2}$$

$$\frac{\partial p}{\partial x} + \phi_s(v_f - v_s) + \Delta \frac{\phi_s(1 - 2\chi \phi_f)}{\phi_f} \frac{\partial \phi_f}{\partial x} = 0, \tag{B.3}$$

$$\frac{\partial \phi_s \sigma_s}{\partial x} - \frac{\partial p}{\partial x} = 0, \tag{B.4}$$

$$\sigma_s = \frac{1 - \phi_s}{\phi_s} \lambda_s + \frac{1 - \phi_s^2}{\phi_s}, \tag{B.5}$$

where $\sigma_s$ is a shorthand for the normal stress component $\sigma_{sxx}$, and the last equation has come from Eq. (33) for 1D strain $\partial u_s / \partial \hat{x}$ and solid expansion $J = 1 + \partial u_s / \partial \hat{x} = 1/\phi_s$. From Eqs. (B.2, B.3, B.4), we eliminate $v_s$ and $p$ and express the fluid velocity $v_f$ in terms of the porosity $\phi_f$:

$$v_f = V_0 + \left[ \sigma_s + \phi_s \sigma_s' - \Delta \frac{\phi_s(1 - 2\chi \phi_f)}{\phi_f} \right] \frac{\partial \phi_f}{\partial x}, \tag{B.6}$$

Where $\sigma_s' = d\sigma_s/d\phi_s$ is a known function of $\phi_s$. Substituting this into Eq. (B.1) and noting $\phi_s = 1 - \phi_f$, we end up with a second-order partial differential equation (PDE) for $\phi_f(x, t)$, which we will not write out explicitly for its algebraic complexity.

To solve the PDE for $\phi_f$, we need the initial condition $\phi_f = \phi_{f0}$ and two boundary conditions. The downstream boundary of the gel layer is fixed in space: $v_s = 0$ at $x = 1$. At the upstream boundary $x = x_i(t)$, the interfacial condition Eq. (38) is simplified to

$$V_0 - v_s = -\eta[\phi_s \sigma_s + m(\ln \phi_f + \phi_s + \chi \phi_s^2)]. \tag{B.7}$$

Through Eqs. (B.2, B.6), these two condition can be converted to BCs for $\phi_f$:

$$\text{at } x = 1 : \left[ \frac{\phi_f}{\phi_s} \sigma_s + \phi_f \sigma_s' - \Delta(1 - 2\chi \phi_f) \right] \frac{\partial \phi_f}{\partial x} = V_0, \tag{B.8}$$

$$\text{at } x = x_i : \left[ \frac{\phi_f}{\phi_s} \sigma_s + \phi_f \sigma_s' - \Delta(1 - 2\chi \phi_f) \right] \frac{\partial \phi_f}{\partial x} + \eta[\phi_s \sigma_s + m(\ln \phi_f + \phi_s + \chi \phi_s^2)] = 0. \tag{B.9}$$

To discretize the PDE using finite difference over the deforming interval $x \in [x_i(t), 1]$, we adopt a Lagrangian grid that uniformly divides the reference state of the solid network, i.e., the dry polymer, and moves with the local velocity $v_s$ of the solid network. Thus, the grid size can be updated dynamically according to the local solid expansion $J = 1/\phi_s$. Another notable feature is that the time derivative $d/dt$ in the Lagrangian frame is a material derivative, and Eq. (B.1) must be transformed to the following for solution:

$$\frac{d\phi_f}{dt} - v_s \frac{\partial \phi_f}{\partial x} + \frac{\partial \phi_f v_f}{\partial x} = 0. \tag{B.10}$$

We use the Crank-Nicolson method to solve Eqs. (B.6, B.8, B.9, B.10). Convergence with respect to the grid size and time step has been confirmed by numerical experiments.

For the spherical hydrogel shell in Section 3.2, the curvilinear geometry complicates the mathematical formulation somewhat because the strain and stress tensors now have

two nontrivial diagonal components, in the radial and azimuthal directions. First, let us simplify the continuity and momentum equations for the spherical symmetry:

$$\frac{\partial \phi_f}{\partial t} + \frac{1}{r^2}\frac{\partial(\phi_f v_f r^2)}{\partial r} = 0, \tag{B.11}$$

$$(v_f \phi_f + v_s \phi_s) = \frac{Q}{4\pi r^2}, \tag{B.12}$$

$$\frac{\partial p}{\partial r} + \phi_s(v_f - v_s) + \Delta\frac{\phi_s(1 - 2\chi\phi_f)}{\phi_f}\frac{\partial \phi_f}{\partial r} = 0, \tag{B.13}$$

$$\frac{\partial \phi_s \sigma_r}{\partial r} + 2\phi_s\frac{\sigma_r - \sigma_\theta}{r} - \frac{\partial p}{\partial r} = 0, \tag{B.14}$$

where $Q(t) = 4\pi a_i^2 V(t) = 2\pi A^3\sqrt{t}$ is the flux at the inner surface of the gel shell (see Eq. 41), and $\sigma_r$ and $\sigma_\theta$ are the radial and azimuthal normal stress components.

The neo-Hookean constitutive equation reduces to

$$\sigma_r = \frac{1}{J}(e_r^2 + 2e_r) + \lambda_s(J - 1), \tag{B.15}$$

$$\sigma_\theta = \frac{1}{J}(e_\theta^2 + 2e_\theta) + \lambda_s(J - 1), \tag{B.16}$$

with the strain components $e_r = \partial u_r/\partial \hat{r}$ and $e_\theta = u_r/\hat{r}$, and the Jacobian $J = 1/\phi_s$. Compared to the 1D planar formulation, the solid stresses are function of $\phi_s$, the displacement $u_r$ and the coordinate $r$. Therefore, we need one more equation $du_r/dt = v_s$ to complete the system. On both surfaces of the gel shell, we impose the same BC of Eq. (B.7).

Similarly to the planar 1D case, we eliminate $v_s$ and $p$ from Eqs. (B.12–B.14) to obtain the radial fluid velocity

$$v_f = \frac{Q}{4\pi r^2} - \frac{\partial \phi_s \sigma_r}{\partial r} - 2\phi_s\frac{\sigma_r - \sigma_\theta}{r} - \Delta\frac{\phi_s(1 - 2\chi\phi_f)}{\phi_f}\frac{\partial \phi_f}{\partial r}. \tag{B.17}$$

From $v_f$, one easily obtains $v_s$ from Eq. (B.12), and in turn the solid displacement $u_r$. Furthermore, we transform the solvent continuity Eq. (B.11) to a Lagrangian form suitable for the finite-difference grid fixed on the solid network:

$$\frac{d\phi_f}{dt} - v_s\frac{\partial \phi_f}{\partial r} + \frac{1}{r^2}\frac{\partial(\phi_f v_f r^2)}{\partial r} = 0. \tag{B.18}$$

By substituting Eq. (B.17) into Eq. (B.18), we obtain a second-order PDE for $\phi_f(r, t)$, which is solved together with the BC of Eq. (B.7) by the Crank-Nicolson method. The only difference from the 1D planar case is that the grid size can no longer be updated according to the local $\phi_s$. Instead, the grid movement must be explicitly computed according to the solid displacement $u_r$.

# Appendix C  Parameter estimation for swelling of gel layer

In presenting results in the main text, we have omitted the overbar for dimensionless groups since the discussion does not concern dimensional parameters. In this appendix, however, both types are present. Thus, we revert temporarily to using an overbar to distinguish dimensionless parameters from dimensional ones.

The dimensionless model parameters of Table 1 can be chosen on the basis of the experiment of Yoon *et al.* [64] and previous modeling of Hong *et al.* [19]. First, we choose $\bar{\lambda}_s = 1.94$ to match the Poisson ratio of 0.33 given by Yoon *et al.* [64]. Then we select $\chi = 0.2$ as a value for typical gels with large swelling ratios [19]. The parameter $\bar{m} = 8.0$, representing the chemical potential jump that triggers the swelling, is fitted to the equilibrium interfacial displacement $\bar{u}_{s1} = 0.8$ in the experiment of Yoon *et al.* [64].

For the parameter $\bar{\Delta} = \mu D/(\mu_s k^*)$, the viscosity of the solvent (water) and the modulus of the polymer network can be taken directly from Yoon *et al.* [64]: $\mu = 10^{-3}$ Pa $\cdot$ s, $\mu_s = 10^3$ Pa. From the average pore size $r = 4.8$ nm [64], we have $k^* = 2r^2/9 = 5.12 \times 10^{-18}$ $m^2$. The diffusivity $D$, however, cannot be taken directly from the value $D_Y$ suggested by Yoon *et al.* [64], for the following differences between the two studies:

- Yoon *et al.* did not include the mixing energy $W_m$ in our Eq. (1) and in Hong *et al.* [19]. Their "chemical potential" is essentially Hong *et al.*'s osmotic pressure.

- Yoon *et al.* adopted a linear elastic model for the stress of the whole gel, whereas we have the neo-Hookean model for the stress $\boldsymbol{\sigma}_s$ of the polymer network, which contributes to the gel mechanics in the form of the Terzaghi stress (Eq. 15).

Thus, Yoon *et al.*'s diffusivity $D_Y$ appears in the following unsteady diffusion equation, which has been converted from their Eq. (11) in the undeformed reference frame to the current deformed frame, and rendered in our notation to facilitate comparison:

$$\frac{\partial \phi_f}{\partial t} = \frac{D_Y}{(1 - \phi_f)^2} \frac{\partial^2 \phi_f}{\partial x^2} + \frac{3D_Y}{(1 - \phi_f)^3} \left( \frac{\partial \phi_f}{\partial x} \right)^2. \tag{C.1}$$

On the other hand, our formalism leads to

$$\frac{\partial \phi_f}{\partial t} = D_e(\phi_f) \frac{\partial^2 \phi_f}{\partial x^2} + \frac{dD_e(\phi_f)}{d\phi_f} \left( \frac{\partial \phi_f}{\partial x} \right)^2, \tag{C.2}$$

where the effective diffusivity $D_e(\phi_f)$ depends not only on the Fickian diffusivity $D$ of Eq. (5), but also on the permeability $k(\phi_f) = k^* \phi_f/(1 - \phi_f)$ (Eq. 10) and the two Lamé constants $\lambda_s$ and $\mu_s$ of the neo-Hookean model (Eq. 16):

$$D_e(\phi_f) = \frac{k}{\mu} [\lambda_s + 2(1 - \phi_f)\mu_s](1 - \phi_f) + D(1 - 2\chi\phi_f)(1 - \phi_f). \tag{C.3}$$

It is thus impossible to link our $D$ to $D_Y$ generally. In the following, we establish a rough linkage by using parameter values and solutions in Section 3.1 of the main paper.

The solutions of Fig. 3 show $\phi(x)$ profiles at different times, from which we can estimate representative magnitudes of $\partial^2 \phi_f/\partial x^2$ and $(\partial \phi_f/\partial x)^2$. Plugging these values into Eqs. (C.1) and (C.2) and equating their right-hand sides, we can estimate $D$ in our model from $D_Y$ of Yoon *et al.* [64]. More specifically, the fluid fraction $\phi_f$ increases from the initial $\phi_{f0} = 0.01$ to the equilibrium value of $\phi_{f\infty} = 0.44$ in time, while the thickness of the gel layer swells from $L_0$ to $1.8L_0$ (Fig. 3). Taking the "mid-points" of these ranges, we use $\phi_f = 0.22$ as a representation porosity, and $\delta\phi_f = 0.22$ as the variation of $\phi_f$ over a thickness of $1.4L_0$, such that $\partial\phi_f/\partial x \sim \delta\phi_f/(1.4L_0)$, $\partial^2\phi_f/\partial x^2 \sim \delta\phi_f/(1.4L_0)^2$. Inserting these into Eqs. (C.1) and (C.2), and using the following parameters: $\mu = 10^{-3}$ Pa·s, $\lambda_s = 1.94 \times 10^3$ Pa, $\mu_s = 10^3$ Pa, $k^* = 5.12 \times 10^{-18}$ m$^2$, $D_Y = 1.5 \times 10^{-11}$m$^2$/s (all from Yoon *et al.*'s experiment [64]), and $\chi = 0.2$ (from Hong *et al.*'s model [19]), we have $D = 8.8 \times 10^{-11}$m$^2$/s, and in turn $\bar{\Delta} = \mu D/(\mu_s k^*) = 17.2$.

By convention, the solid strain is measured relative to a reference state corresponding to the dry polymers [19]. But Yoon *et al.* did not state explicitly whether their

displacement was relative to a dry polymer layer or a pre-swelled gel layer. We have taken the initial state to be a dense gel with initial uniform porosity $\phi_{f0} = 0.01$, close to the dry state. This corresponds to an initial $\bar{m} = 1.15 \times 10^{-2}$, and the swelling is triggered by abruptly raising $\bar{m}$ to 8.

# References

[1] O. Okay, General properties of hydrogels, in: Hydrogel Sensors and Actuators, Springer, 2009, pp. 1–14.

[2] L. Ionov, Hydrogel-based actuators: possibilities and limitations, Mater. Today 17 (10) (2014) 494–503.

[3] E. W. K. Young, Cells, tissues, and organs on chips: challenges and opportunities for the cancer tumor microenvironment, Integr. Biol. 5 (2013) 1096–1109. doi:10.1039/C3IB40076J.

[4] H. Liu, Y. Wang, K. Cui, Y. Guo, X. Zhang, J. Qin, Advances in hydrogels in organoids and organs-on-a-chip, Adv. Mater. 31 (50) (2019) 1902042.

[5] E. L. Doherty, W. Y. Aw, A. J. Hickey, W. J. Polacheck, Microfluidic and organ-on-a-chip approaches to investigate cellular and microenvironmental contributions to cardiovascular function and pathology, Front. Bioeng. Biotechnol. 9 (2021) 624435.

[6] L. Dong, A. K. Agarwal, D. J. Beebe, H. Jiang, Adaptive liquid microlenses activated by stimuli-responsive hydrogels, Nature 442 (7102) (2006) 551–554.

[7] T. Lopez-Leon, A. Fernandez-Nieves, Macroscopically probing the entropic influence of ions: deswelling neutral microgels with salt, Phys. Rev. E 75 (2022) 011801.

[8] M. C. Koetting, J. T. Peters, S. D. Steichen, N. A. Peppas, Stimulus-responsive hydrogels: theory, modern advances, and applications, Mater. Sci. Eng. 93 (2015) 1–49.

[9] O. Erol, A. Pantula, W. Liu, D. H. Gracias, Transformer hydrogels: a review, Adv. Mater. Technol. 4 (2019) 1900043.

[10] M. D. Butler, T. D. Montenegro-Johnson, The swelling and shrinking of spherical thermo-responsive hydrogels, J. Fluid Mech. 947 (2022) A11.

[11] D. J. Beebe, J. S. Moore, J. M. Bauer, Q. Yu, R. H. Liu, C. Devadoss, B.-H. Jo, Functional hydrogel structures for autonomous flow control inside microfluidic channels, Nature 404 (6778) (2000) 588–590.

[12] S. Niroumandi, M. Shojaeifard, M. Baghani, On single and multiple pH-sensitive hydrogel micro-valves: A 3D transient fully coupled fluid-solid interaction study, Transp. Porous Med. 142 (2022) 295–316.

[13] F. Han, X. Xie, T. Wang, C. Cao, J. Li, T. Sun, H. Liu, S. Geng, Z. Wei, J. Li, F. Xu, Wearable hydrogel-based epidermal sensor with thermal compatibility and long term stability for smart colorimetric multi-signals monitoring, Adv. Healthcare Mater. 12 (2023) 2201730.

[14] Y. Zhao, A. Kim, G. Wan, B. C. K. Tee, Design and applications of stretchable and self-healable conductors for soft electronics, Nano Converg. 6 (2019) 25.

[15] D. Jiao, Q. L. Chu, C. Y. Li, Q. Zheng, Z. L. Wu, Programmable morphing hydrogels for soft actuators and robots: from structure designs to active functions, Acc. Chem. Res. 55 (2022) 1533–1545.

[16] W. J. Polacheck, J. L. Charest, R. D. Kamm, Interstitial flow influences direction of tumor cell migration through competing mechanisms, Proc. Natl. Acad. Sci. U.S.A. 108 (27) (2011) 11115–11120. doi:10.1073/pnas.1103581108.

[17] W. J. Polacheck, R. Li, S. G. M. Uzel, R. D. Kamm, Microfluidic platforms for mechanobiology, Lab Chip 13 (2013) 2252–2267.

[18] M. B. Chen, J. A. Whisler, J. Fröse, C. Yu, Y. Shin, R. D. Kamm, On-chip human microvasculature assay for visualization and quantification of tumor cell extravasation dynamics, Nat. Protoc. 12 (5) (2017) 865–880.

[19] W. Hong, X. Zhao, J. Zhou, Z. Suo, A theory of coupled diffusion and large deformation in polymeric gels, J. Mech. Phys. Solids 56 (5) (2008) 1779–1793.

[20] M. Doi, Gel dynamics, J. Phys. Soc. Jpn. 78 (5) (2009) 052001.

[21] S. A. Chester, L. Anand, A thermo-mechanically coupled theory for fluid permeation in elastomeric materials: Application to thermally responsive gels, J. Mech. Phys. Solids 59 (10) (2011) 1978–2006.

[22] M. Engelsberg, W. Barros, Free-evolution kinetics in a high-swelling polymeric hydrogel, Phys. Rev. E 88 (2013) 062602.

[23] A. Lucantonio, P. Nardinocchi, L. Teresi, Transient analysis of swelling-induced large deformations in polymer gels, J. Mech. Phys. Solids 61 (1) (2013) 205–218.

[24] N. Bouklas, C. M. Landis, R. Huang, A nonlinear, transient finite element method for coupled solvent diffusion and large deformation of hydrogels, J. Mech. Phys. Solids 79 (2015) 21–43.

[25] T. Bertrand, J. Peixinho, S. Mukhopadhyay, C. W. MacMinn, Dynamics of swelling and drying in a spherical gel, Phys. Rev. Appl. 6 (2016) 064010.

[26] M. Curatolo, P. Nardinocchi, E. Puntel, L. Teresi, Transient instabilities in the swelling dynamics of a hydrogel sphere, J. Appl. Phys. 122 (14) (2017) 145109.

[27] A. D. Drozdov, J. deClaville Christiansen, A simplified model for equilibrium and transient swelling of thermo-responsive gels, J. Mech. Behav. Biomed. Mater. 75 (2017) 20–32.

[28] M. G. Hennessy, A. Münch, B. Wagner, Phase separation in swelling and deswelling hydrogels with a free boundary, Phys. Rev. E 101 (2020) 03251.

[29] G. L. Celora, M. G. Hennessy, A. Münch, B. Wagner, S. L. Waters, A kinetic model of a polyelectrolyte gel undergoing phase separation, J. Mech. Phys. Solids 160 (2022) 104771.

[30] M. Dolega, G. Zurlo, M. Le Goff, M. Greda, C. Verdier, J.-F. Joanny, G. Cappello, P. Recho, Mechanical behavior of multi-cellular spheroids under osmotic compression, J. Mech. Phys. Solids 147 (2021) 104205.

[31] J. J. Webber, M. G. Worster, A linear-elastic-nonlinear-swelling theory for hydrogels. Part 1. Modelling of super-absorbent gels, J. Fluid Mech. 960 (2023) A37.

[32] J. J. Webber, M. G. Worster, A linear-elastic-nonlinear-swelling theory for hydrogels. Part 2. Displacement formulation, J. Fluid Mech. 960 (2023) A38.

[33] J. A. Ochoa-Tapia, S. Whitaker, Momentum transfer at the boundary between a porous medium and a homogeneous fluid - I. Theoretical development, Int. J. Heat Mass Transfer 38 (1995) 2635–2646.

[34] K. Vafai, Handbook of Porous Media, CRC Press, 2015.

[35] P. Angot, B. Goyeau, J. A. Ochoa-Tapia, Asymptotic modeling of transport phenomena at the interface between a fluid and a porous layer: Jump conditions, Phys. Rev. E 95 (2017) 063302.

[36] C. W. MacMinn, E. R. Dufresne, J. S. Wettlaufer, Large deformations of a soft porous material, Phys. Rev. Appl. 5 (4) (2016) 044020. doi:10.1103/PhysRevApplied.5.044020.

[37] B. Alazmi, K. Vafai, Analysis of fluid flow and heat transfer interfacial conditions between a porous medium and a fluid layer, Int. J. Heat Mass Transfer 44 (2001) 1735–1749.

[38] M. Minale, Momentum transfer within a porous medium. I. Theoretical derivation of the momentum balance on the solid skeleton, Phys. Fluids 26 (2014) 123101.

[39] M. Minale, Momentum transfer within a porous medium. II. Stress boundary condition, Phys. Fluids 26 (2014) 123102.

[40] Y.-N. Young, Y. Mori, M. J. Miksis, Slightly deformable Darcy drop in linear flows, Phys. Rev. Fluids 4 (2019) 063601.

[41] J. J. Feng, Y.-N. Young, Boundary conditions at a gel-fluid interface, Phys. Rev. Fluids 5 (2020) 124304.

[42] L. Li, J. Zhang, Z. Xu, Y.-N. Young, J. J. Feng, P. Yue, An arbitrary Lagrangian-Eulerian method for simulating interfacial dynamics between a hydrogel and a fluid, J. Comput. Phys. 451 (2022) 110851.

[43] Z. Xu, J. Zhang, Y.-N. Young, P. Yue, J. J. Feng, A comparison of four boundary conditions for the fluid-hydrogel interface, Phys. Rev. Fluids 7 (2022) 093301.

[44] Y. Li, O. S. Sariyer, A. Ramachandran, S. Panyukov, M. Rubinstein, E. Kumacheva, Universal behavior of hydrogels confined to narrow capillaries, Sci. Rep. 5 (2015) 17017.

[45] Z. Xu, P. Yue, J. J. Feng, Poroelastic modeling reveals the cooperation between two mechanisms for albuminuria, J. R. Soc. Interface 20 (2023) 20220634.

[46] D. Kim, D. J. Beebe, Hydrogel-based reconfigurable components for microfluidic devices, Lab Chip 7 (2007) 193–198.

[47] D. Kim, D. J. Beebe, A bi-polymer micro one-way valve, Sens. Actuator A Phys. 136 (2007) 426–433.

[48] L. D'Eramo, B. Chollet, M. Leman, E. Martwong, M. Li, H. Geisler, J. Dupire, M. Kerdraon, C. Vergne, F. Monti, Y. Tran, P. Tabeling, Microfluidic actuators based on temperature-responsive hydrogels, Microsyst. Nanoeng. 4 (2018) 17069.

[49] M. J. Lundahl, V. Klar, L. Wang, M. Ago, O. J. Rojas, Spinning of cellulose nanofibrils into filaments: A review, Ind. Eng. Chem. Res. 56 (1) (2017) 8–19.

[50] L. Bai, L. Liu, M. Esquivel, B. L. Tardy, S. Huan, X. Niu, S. Liu, G. Yang, Y. Fan, O. J. Rojas, Nanochitin: Chemistry, structure, assembly, and applications, Chem. Rev. 122 (13) (2022) 11604–11674.

[51] M. Bacca, R. M. McMeeking, A viscoelastic constitutive law for hydrogels, Meccanica 52 (2017) 3345–3355.

[52] M. L. Huggins, Solutions of long chain compounds, J. Chem. Phys. 9 (5) (1941) 440–440. doi:10.1063/1.1750930.

[53] P. J. Flory, Thermodynamics of high polymer solutions, J. Chem. Phys. 10 (1) (1942) 51–61. doi:10.1063/1.1723621.

[54] R. B. Bird, W. E. Stewart, E. N. Lightfoot, Transport Phenomena, 2nd Edition, Wiley, 2007.

[55] E. L. Cussler, Diffusion: Mass Transfer in Fluid Systems, 3rd Edition, Cambridge University Press, 2009.

[56] N. Annabi, J. W. Nichol, X. Zhong, C. Ji, S. Koshy, A. Khademhosseini, F. Dehghani, Controlling the porosity and microarchitecture of hydrogels for tissue engineering, Tissue Eng. Part B 16 (4) (2010) 371–383.

[57] A. Salerno, R. Borzacchiello, P. A. Netti, Pore structure and swelling behavior of porous hydrogels prepared via a thermal reverse-casting technique, J. Appl. Polym. Sci. 122 (2011) 3651–3660.

[58] S. Kovačič, M. S. Silverstein, Superabsorbent, high porosity, PAMPS-based hydrogels through emulsion templating, Macromol. Rapid Commun. 37 (2016) 1814–1819.

[59] F. A. L. Dullien, Chapter 3: Single-phase transport phenomena in porous media, in: Porous Media: Fluid Transport and Pore Structure, 2nd Edition, Academic Press, San Diego, 1992, pp. 237–317.

[60] R. E. Caflisch, J. Rubinstein, Chapter 6: Flow in porous media, in: Lectures on the Mathematical Theory of Multi-phase Flow, New York University, 1986, pp. 64–73.

[61] S. S. L. Peppin, J. A. W. Elliott, M. G. Worster, Pressure and relative motion in colloidal suspensions, Phys. Fluids 17 (5) (2005) 053301. doi:10.1063/1.1915027.

[62] D. R. Hewitt, J. S. Nijjer, M. G. Worster, J. A. Neufeld, Flow-induced compaction of a deformable porous medium, Phys. Rev. E 93 (2) (2016) 023116.

[63] O. Coussy, Poromechanics, Wiley, 2004.

[64] J. Yoon, S. Cai, Z. Suo, R. C. Hayward, Poroelastic swelling kinetics of thin hydrogel layers: comparison of theory and experiment, Soft Matter 6 (23) (2010) 6004.

[65] S. A. Chester, L. Anand, A coupled theory of fluid permeation and large deformations for elastomeric materials, J. Mech. Phys. Solids 58 (2010) 1879–1906.

[66] A. D. Drozdov, A. A. . Papadimitriou, J. H. M. Liely, C.-G. Sanporean, Constitutive equations for the kinetics of swelling of hydrogels, Mech. Mater. 102 (2016) 61–73.

[67] Y. Liu, H. Zhang, J. Zhang, Y. Zheng, Transient swelling of polymeric hydrogels: A new finite element solution framework, Int. J. Solids Struct. 80 (2016) 246–260.

[68] Z. Xu, P. Yue, J. J. Feng, Estimating the interfacial permeability for flow into a poroelastic medium, Soft Matter (submitted 2024).

[69] C. Carrick, M. Ruda, B. Pettersson, P. T. Larsson, L. Wågberg, Hollow cellulose capsules from $CO_2$ saturated cellulose solutions—their preparation and characterization, RSC Adv. 3 (7) (2013) 2462.

[70] K. Mystek, H. Li, T. Pettersson, H. Françon, A. J. Svagan, P. A. Larsson, L. Wågberg, Wet-expandable capsules made from partially modified cellulose, Green Chem. 22 (14) (2020) 4581–4592.

[71] P. S. Epstein, M. S. Plesset, On the stability of gas bubbles in liquid-gas solutions, J. Chem. Phys. 18 (1950) 1505–1509.

[72] D. M. J. P. Manley, Change of size of air bubbles in water containing a small dissolved air content, Br. J. Appl. Phys. 11 (1) (1960) 38–42.

[73] U. Lācis, Y. Sudhakar, S. Pasche, S. Bagheri, Transfer of mass and momentum at rough and porous surfaces, J. Fluid Mech. 884 (2020) A21.